Impact of far-field glacially-induced stresses on fault stability in the eastern Paris Basin

Adrien Damon, Stéphane Mazzotti, Philippe Vernant, Rémi Vachon, Juliette Grosset, Frédéric Ego, David Baumont

Tectonophysics 864 (2023) 230035

Contents lists available at ScienceDirect

Tectonophysics

journal homepage: www.elsevier.com/locate/tecto

Impact of far-field glacially-induced stresses on fault stability in the eastern Paris Basin

Adrien Damon [a,b,*], Stéphane Mazzotti [b], Philippe Vernant [b], Rémi Vachon [c], Juliette Grosset [b], Frédéric Ego [a], David Baumont [d]

[a] ANDRA, 7, rue Jean-Monnet, 92298 Châtenay-Malabry cedex, France
[b] Géosciences Montpellier, CNRS, Université de Montpellier, 34000 Montpellier, France
[c] Department of Earth Sciences (MPT), Geocentrum, Villavägen 16, 752 36 Uppsala, Sweden
[d] Seister S.A.S., Immeuble Le Quartz, 58 chemin de la justice, 92290 Châtenay-Malabry, France

ARTICLE INFO

Keywords:
Seismotectonics
Glacial isostasy
Fault stability
Stable continental region
Paris Basin

ABSTRACT

Stable Continental Regions (SCR) feature very low seismicity levels, but historical seismicity reveals that these areas can experience large damaging earthquakes of magnitude up to $M_w \approx 7$, on faults that were previously undocumented or thought to be stable. Glacial Isostatic Adjustment (GIA) is commonly considered as a factor of SCR deformation and stress perturbations that can trigger fault failure in formerly glaciated areas. Studies suggest that fault reactivation due to GIA may not only be restricted to glaciated areas, but could also occur in their periphery, several hundreds of kilometers away from the former glaciations. In this study, we model GIA associated to the Alpine, Massif Central, Celtic and Scandinavian glaciations from the last glacial cycle, in order to estimate the impact of this process on fault stability in the eastern Paris Basin, an area featuring very low strain rates and seismic activity, but of particular interest due to the proposed construction of a radioactive waste disposal facility. Our computations predict stress perturbations far (hundreds of kilometers away) from the ice loads, of similar amplitude to those in areas where fault reactivation has been observed (1–8 MPa at LGM, 0.8–2 MPa at present-day in our study area). We also show that the interaction between several GIA systems can impact the timing of maximum fault destabilization in a different way than common models considering only a single ice load. The computed far-field glacially-induced stress perturbations remain small compared to ambient crustal stresses, but they are large enough to potentially destabilize faults close to Andersonian geometries, with known faults in the eastern Paris Basin meeting these criteria, mainly in the Marne and Saint-Martin-de-Bossenay fault systems. Yet, there is no known evidence of Quaternary fault activity in the Paris Basin, and discrepancies between the localization of potentially unstable faults due to GIA and seismically active areas in northern France suggests that other processes must be at play.

1. Introduction

Stable Continental Regions (SCR) are defined as continental areas that have not undergone orogenic activities or anorogenic intrusions since the early Cretaceous, nor rifting or major extension since the Paleogene (Johnston, 1989; Johnston et al., 1994). A direct corollary of this definition in that SCR feature very to extremely low levels of present-day deformation and seismicity. Yet, these regions can experience large damaging earthquakes, such as the 2001, Mw = 7.6, Bhuj (India) or 1811–1812, Mw ≈ 7, New Madrid (USA) events (Hough and Page, 2011; Singh et al., 2004). A majority of SCR earthquakes feature peculiar characteristics: a tendency toward shallow depth (0–10 km, upper third of the crust) with surface ruptures (Klose and Seeber, 2007), rupturing of previously undocumented faults in regions of very low background seismicity (Adams et al., 1991), isolated fault activity over very long periods (10^4 to $>10^5$ yr, Clark et al. (2014); Crone et al. (2003)), and triggering or time advance by transient surface processes (Calais et al., 2010; Hough et al., 2003).

These attributes of large SCR earthquakes raise major questions regarding the geodynamic processes leading to fault loading, triggering mechanisms, and long-term variations of such seismic activity (Calais et al., 2016; Mazzotti, 2007; Talwani, 2017). Proposed forcing

* Corresponding author at: ANDRA, 7, rue Jean-Monnet, 92298 Châtenay-Malabry cedex, France.
E-mail address: adrien.damon@umontpellier.fr (A. Damon).

https://doi.org/10.1016/j.tecto.2023.230035
Received 17 November 2022; Received in revised form 1 August 2023; Accepted 4 September 2023
Available online 9 September 2023

mechanisms include mantle dynamics (Forte et al., 2007), crustal and lithospheric mantle density contrasts (Jackson and McKenzie, 2022), erosional unloading (Calais et al., 2010), or Glacial Isostatic Adjustment (GIA) (Wu and Johnston, 2000). The latter is commonly proposed as a factor of intraplate deformation that could trigger fault activity in formerly glaciated areas (Mörner, 1978; Muir-Wood, 2000; Stewart et al., 2000). Although it remains debated, GIA is also considered as a potential triggering mechanism for fault activity in regions at the periphery of the past ice loads such as northern central Europe or central North America (Brandes et al., 2012, 2015; Grollimund and Zoback, 2001). Numerical modeling suggests that GIA can impact fault stability and slip rate throughout the glacial cycle (Hampel et al., 2009) and that large sets of pre-existing faults may be destabilized under GIA effects (Steffen and Steffen, 2021), in and out of the formerly glaciated areas.

These various theoretical questions also raise significant issues for estimating seismic hazard in SCR regions (Stein and Mazzotti, 2007). This is especially true for high-stake structures such as nuclear power plants or waste-disposal facilities, which require hazard assessments that consider very low probability events (Fenton et al., 2006; Johnston et al., 1994). Such extreme and isolated events may not be recorded in earthquake catalogs nor in fault and tectonic evidence databases. Thus, studies of potential fault activity under various driving mechanisms constitute an important tool for both geodynamics understanding and hazard applications in SCR.

In this study, we test the potential impact of GIA-induced stress perturbations on fault activity in the eastern Paris Basin, France (Fig. 1). This region is of particular interest due to the proposed construction of a deep geological radioactive waste disposal facility. Although the eastern Paris Basin is characterized by an extremely low seismicity level and no known recent fault activity (see Section 2), it is located at the periphery of several ice systems from the Last Glacial Maximum (LGM): the relatively small Alpine and Massif Central glaciers (200 and 350 km away, respectively), and the major Celtic and Fennoscandian ice sheets (550 and 750 km away, respectively). The sediment basin and basement of the eastern Paris Basin are affected by several fault systems, including both structures restricted to the sedimentary cover and deep-rooted Variscan and Cenozoic structures (see Section 2), that can be tested for potential reactivation by GIA. This configuration offers an opportunity for testing the interactions of several GIA systems on a set of well-defined pre-existing fault structures in a far-field context relative to ice loads. To do so, we model the LGM and present-day GIA effects, expressed as stress perturbations, in the eastern Paris Basin associated with the Alpine, Massif Central, Celtic and Fennoscandian ice systems. In particular, we test the importance of integrating lateral heterogeneities of lithosphere rigidity in GIA computations, according to regional estimates based on structural, thermal, and strain rate data over Western Europe. The computed stress perturbations are combined with models of ambient stress fields and projected onto various fault geometries using a Coulomb Failure Stress (CFS) approach, in order to identify potentially destabilized faults in our study area.

2. Geological context

The Paris Basin (Fig. 1a) corresponds to the sedimentary cover of a crystalline basement structured during the Cadomian (650–500 Ma) and Variscan (420–280 Ma) orogenies (Cazes et al., 1986; Matte and Hirn, 1988). The sedimentation started during the Permian (250 Ma) and the latest sediments are from the Pliocene (5.3–2.6 Ma) (Beccaletto et al., 2011; Guillocheau et al., 2000; Mégnien, 1980). The eastern Paris Basin features subvertical (around 80° dip) basement faults (Rossi and Baudouy, 2015) inherited from the Variscan orogeny, such as the Vittel Fault, and grabens formed during the Cenozoic western Europe rifting (40–25 Ma) affecting the sedimentary cover, such as the Gondrecourt and Saint-Dizier grabens (Fig. 1b) (Beccaletto et al., 2011; Mégnien, 1980).

The eastern Paris Basin has experienced three main deformation phases associated with the Pyrenean orogeny (55–25 Ma), the Cenozoic western Europe rifting (40–25 Ma), and the Alpine orogeny (40–15 Ma). Fracturing in relation with these events is reported (Blaise et al., 2022). Fault activity is proposed to have occurred on major basement faults from the Permo-Carboniferous onwards, as well as on NW-SE trending normal faults formed during the Cenozoic western Europe rifting (Guillocheau et al., 2000). No recent deformation or tectonic evidence is observed, suggesting that no major deformation or fault activity have occurred since 15 Ma (André et al., 2010; Blaise et al., 2022). Nowadays, the Paris Basin features a very low seismicity level, with no known

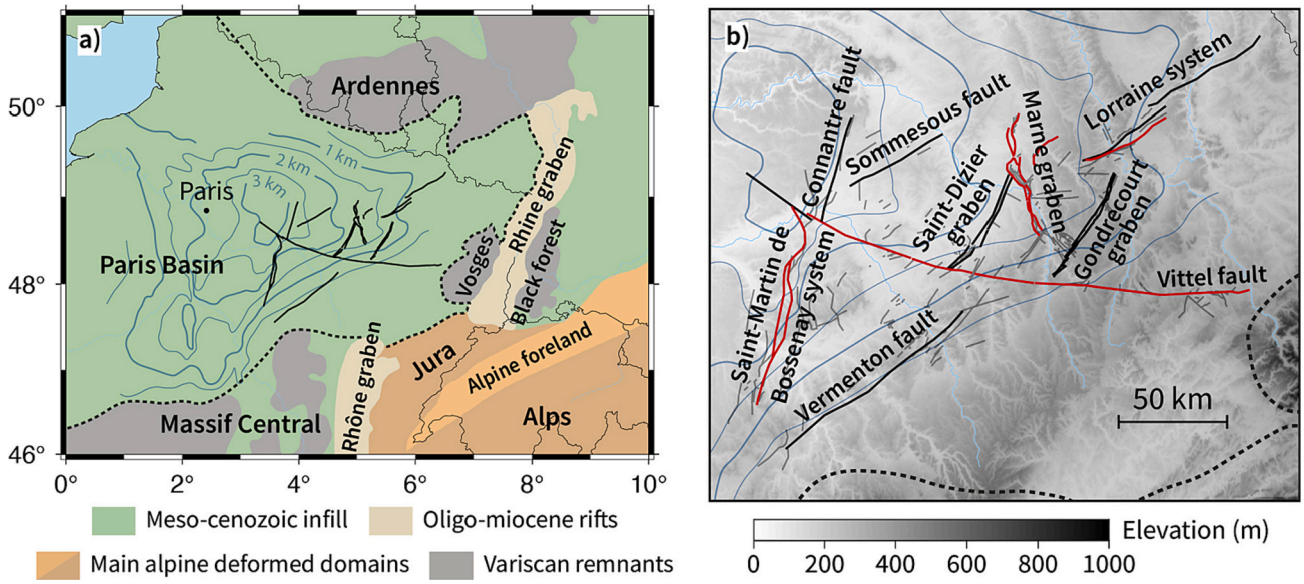

Fig. 1. Structural context of the eastern Paris Basin. Dashed line delineates the border of the Paris Basin, blue contours indicate the thickness of its sedimentary cover (Geological map of France, scale 1:1,000,000, Bureau des Recherches Géologiques et Minières (BRGM), 1996). a) Structural scheme of the Paris Basin region and major fault systems in our study area (black lines). b) Detail of the studied fault network in our study area. Red lines indicate basement faults, faults limited to the sedimentary cover are in black and gray for primary and secondary faults, respectively. (For interpretation of the references to colour in this figure legend, the reader is referred to the web version of this article.)

instrumental or historical earthquake of magnitude $M_w > 4$, and very low level of background seismicity (most of which is associated to anthropic activity, BCSF RENASS (2022), SI-Hex database, Cara et al. (2015)). Geodetic data (GNSS) indicate very small strain rates at the limit of the method resolution, in and around the Paris Basin (Masson et al., 2019).

3. GIA modeling

In order to model the response of the Earth to a glaciation, the Earth is commonly considered as a Maxwell viscoelastic spherical body consisting in an elastic lithosphere over a layered viscoelastic mantle (Peltier, 1974). For ice loads of small spatial extent (less than a few hundreds of kilometers), sphericity can be neglected and planar models produce excellent results compared to spherical models (Wu and Johnston, 1998). In this study, we use two approaches: We follow Wu (2004) approach to compute GIA associated with the large Scandinavian and Celtic ice loads, using a finite-element model that includes spatially variable lithosphere equivalent elastic thickness over a layered mantle viscoelasticity structure (Section 3.2.1). For small ice loads (100–200 km wide) such as the Alps or Massif Central, the GIA response is restricted to the upper mantle (<200 km depth (Steffen et al., 2015)) and a thin elastic plate approach, consisting in an elastic lithosphere overlying a uniform viscous upper mantle, is suitable (see supplementary Section S2.2 and Section 3.2.2). This second approach requires short computation times and allows us to extensively test the impact of lithosphere rigidity parameters on computations in our study area (Section S1.2 of the supplementary material).

3.1. Ice loads

The last major glaciations in western Europe reached their maximums around 88, 60 and 23 ka (Patton et al., 2017). Due to the typical mantle relaxation time about 10^4 yr (Haskell, 1937), we consider that GIA effects are nearly over after a few tens of kyr (residual effects of 20% or less, Vachon et al., 2022). Thus, in order to study the LGM and present-day states GIA effects, we limit our models to the last glacial period: the Weichselian / Würm glaciation (Fig. 2).

The Scandinavian and Celtic ice sheet models are a reconstruction by Patton et al. (2017) for the last 122.8 kyr. The Scandinavian and Celtic ice sheet dimensions are about 1900 × 1300 km and 1200 × 600 km, respectively. This reconstruction includes three periods of glaciation lasting 10–15 kyr each, with the ice cover reaching a maximum extent at 88.2 ka, 59.8 ka and 23 ka. The maximum ice thickness exceeds 2.25 km on the northern coast of the Gulf of Bothnia and at the center of the Barents Sea (Fig. 2). Each glacial maximum is followed by an almost entire collapse of the ice sheet. During the ultimate deglaciation over Scandinavia, the Barents Sea and the Celtic Isles, ice sheets lasted until 17 to 10 ka. Ice thicknesses are converted into two-dimensional time-dependent surface loads applied at the surface of the Earth model.

The LGM Alpine ice model (Mey et al., 2016) is dated at 21 ka and is about 650 km long by 150–250 km wide, with a 500 m average thickness (up to 2 km in a few major Alpine valleys, Fig. 2). Deglaciation occurred very quickly around 17 ka on a relatively short timescale of 2–3 kyr (Ivy-Ochs et al., 2008; Seguinot et al., 2018). For the Massif Central, we build a simple LGM ice model from local Quaternary ice extent markers (Etlicher and de Goër De Hervé, 1988). The model is composed of 7 glaciers of 10–100 km width and ice thickness of 300 m (Ancrenaz et al., 2020). Due to the proximity of the Massif Central and Alps, and the lack of information on the Massif Central glaciations, we assume the same glaciation history as for the Alps. In both cases, the modeled deglaciation is assumed to be instantaneous at 17 ka.

3.2. GIA and stress perturbations computation

3.2.1. Scandinavian and Celtic ice sheets

The response to Scandinavian and Celtic ice sheets is computed using the methodology of Wu (2004) and Vachon et al. (2022). We take a first order approach and do not include the change in density due to material compression (i.e. internal buoyancy) but we allow for material compressibility (Klemann et al., 2003). This simplification results in variations of <5% in the predicted deformation under the center of the ice load (Schotman et al., 2008). We do not include self-gravitation as it was shown that this process is counteracted by the flat Earth approximation (Amelung and Wolf, 1994; Schotman et al., 2008; Spada et al., 2011). We also do not consider minor processes such as the gravitational attraction of the evolving ice mass. After simplification, the momentum equation becomes Eq. (1), from which we compute the stress perturbations associated with lithosphere bending due to an ice load:

$$\nabla\cdot\sigma - \nabla(u\cdot\rho_0 g_0 \hat{z}) = 0 \quad (1)$$

with σ the stress tensor, u the displacement vector, $\hat{z}$ the along-depth unit vector, ρ_0 and g_0 the density of the Earth material at depth and the gravitational acceleration before deformation. To account for pre-stress advection, we set a spring foundation at the surface of the Earth and at each density contrast of the model, with the spring constant only acting in the vertical direction (Schmidt et al., 2012; Wu, 2004).

We model the solid Earth as a three-dimensional layered box defined by a Maxwell viscoelastic rheology. The model domain is 6150 km in

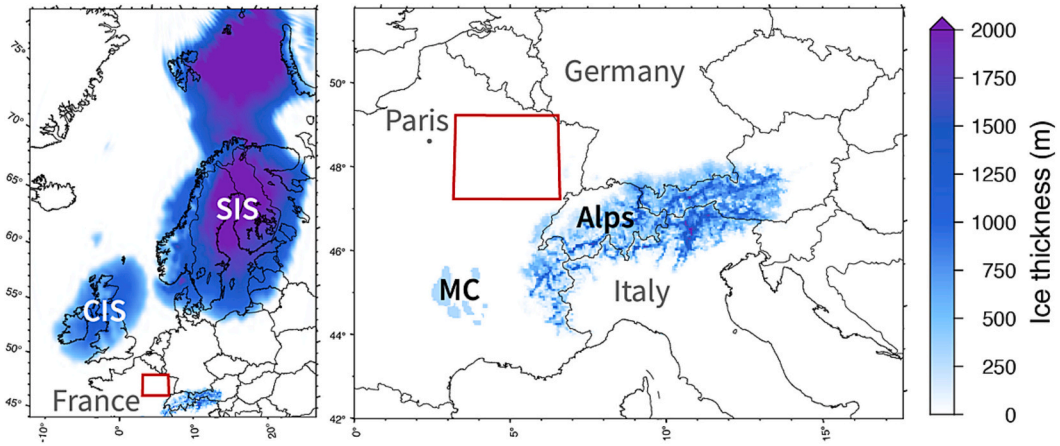

Fig. 2. Ice systems represented as LGM (21 ka) ice thickness (Mey et al., 2016; Patton et al., 2017). The red rectangle is the study zone. CIS = Celtic ice sheet, SIS = Scandinavian ice sheet, MC = Massif Central. (For interpretation of the references to colour in this figure legend, the reader is referred to the web version of this article.)

length, 2800 km in width, and covers the region of northern Europe, incorporating the entire ice model of Patton et al. (2017) and extending in the south to include France and the Paris Basin. The model extends to 2800 km in depth (core-mantle boundary). To avoid boundary effects in the GIA solution, the model is embedded into a half-sphere with a radius that extends to ten times the lateral dimension of the central box, with edges fixed in every direction (Lund, 2005). The elastic lithosphere is discretized by tetrahedra with a mean node spacing of 50 km in the horizontal plane and 12 km in the vertical dimension. In the rest of the center box, elements are 100 km and 350 km in size in the upper and lower mantle, respectively. In total, the model is discretized in ~345,000 quadratic tetrahedral elements, which correspond to 6,400,000 degrees of freedom. We use COMSOL Multiphysics® to solve the momentum equation (Eq. (1)), from 122.8 ka to present-day and with a maximum time step of 100 yr.

3.2.2. Alpine and Massif Central glaciers

Due to the small spatial dimension of the alpine and MC glaciers, we model the response of the lithosphere to ice loading and unloading assuming an elastic thin plate (of thickness T_e) over a viscous substratum (see supplementary Section S2.2). The elastic plate flexure w in response to the ice load is computed with the gFlex code (Wickert, 2015):

$$w(x,y) = w_0 \times kei\left(\frac{\sqrt{x^2+y^2}}{\alpha}\right) \tag{2}$$

with w_0 the maximum deflection due to the vertical stress under the ice load q:

$$w_0 = q\frac{\alpha^2}{2\pi D} \tag{3}$$

The flexural parameter α depends on the flexural rigidity D:

$$\alpha = \left(\frac{D}{\Delta\rho g}\right)^{1/4} \tag{4}$$

and D primarily depending on the lithosphere equivalent elastic thickness T_e:

$$D = \frac{ET_e^3}{12(1-\nu^2)} \tag{5}$$

kei are the zero-order Kelvin function, x and y the distance to the load, $\Delta\rho$ the density difference between the ice load and mantle, g the gravitational acceleration, E Young's modulus, and ν Poisson's ratio (Turcotte and Schubert, 2002; Wickert, 2015).

The Alpine and MC postglacial rebound response is computed assuming an instantaneous ice melt after the LGM at 17 ka (as discussed in Section 3.1, Seguinot et al., 2018). The effect of the upper mantle viscosity is modeled by an exponential decay controlled by a relaxation time τ (Turcotte and Schubert, 2002):

$$w(t) = w \times e^{-t/\tau} \tag{6}$$

Thus, our models mainly depend on the elastic plate thickness T_e, which controls the wavelength and amplitude of the plate deformation, and the characteristic time τ, which controls the temporal evolution of the deformation. Stresses in the elastic plate are computed using Hooke's law, with strain computed as the second spatial derivative of the flexural response of the plate w, based on the Kirchhoff-Love plate theory. In order to consider the maximum GIA stress perturbation, we consider the stress at the top of the elastic plate.

3.3. Lithosphere flexural rigidity

3.3.1. Continental Europe T_e

Continental Europe T_e estimates are based on gravity-topography admittance or coherence methods (Audet, 2014; Kaban et al., 2018) or rheological modeling of the lithosphere (Tesauro et al., 2009a, 2013). These approaches show a large variability in their results (Audet, 2014; Burov and Diament, 1995; Tesauro et al., 2012a) related to the window size for admittance/coherence methods or the parameter assumptions for lithosphere rheology modeling (e.g., use of hypothetical strain rate and crustal composition). In order to test the variability of T_e, we compute rheological models of the European lithosphere integrating variability in rheological, thermal, strain rate, and structural parameters. We estimate T_e from Yield Stress Envelopes (YSE) (Burov and Diament, 1995; Ranalli, 1994) by calculating lithospheric temperatures and yield stresses along depth. We compute a large range of rheological models by testing the thermal properties of the lithosphere (surface heat flow, thermal conductivity), crust and mantle composition, and assumed strain rates (from GNSS measurements). We test every combination of these parameters and only retain those for which the computed geotherm is consistent with estimations based on seismic tomography (Cloetingh et al., 2007; Tesauro et al., 2009b).

In order to take into account heterogeneity over the modeling zone, we define six lithospheric domains based on the mentioned parameters lateral variations (Fig. 3 and Table 1).

- Western Europe (WE) has the thinnest crust (25–35 km) and a high surface heat flow (65–100 mW.m^{-2}), as well as the shallowest lithosphere-asthenosphere boundary (LAB, indicated by the 1200–1300 °C isotherm depth of 100–160 km). This domain has the highest GNSS-derived strain rate (~2 × 10^{-17} s^{-1}). These characteristics suggest a local lithosphere of relativity small rigidity.
- The Eastern European Platform (EEP) corresponds to a large domain of thick crust (40–55 km) covered by 0–2 km thick sediments. The average heat flow is low (40–60 mW.m^{-2}). GNSS-derived strain rates are about 1.6 × 10^{-17} s^{-1}.
- Scandinavia (Sc1 and Sc2 domains) has the thickest crust (32–62 km) and the lowest surface heat flow (20–60 mW.m^{-2}). It corresponds to a continental shield with the deepest obtained LAB at 110–300 km depth and low GNSS-derived strain rates (~2 × 10^{-16} s^{-1}). These features suggest a relatively strong local lithosphere.

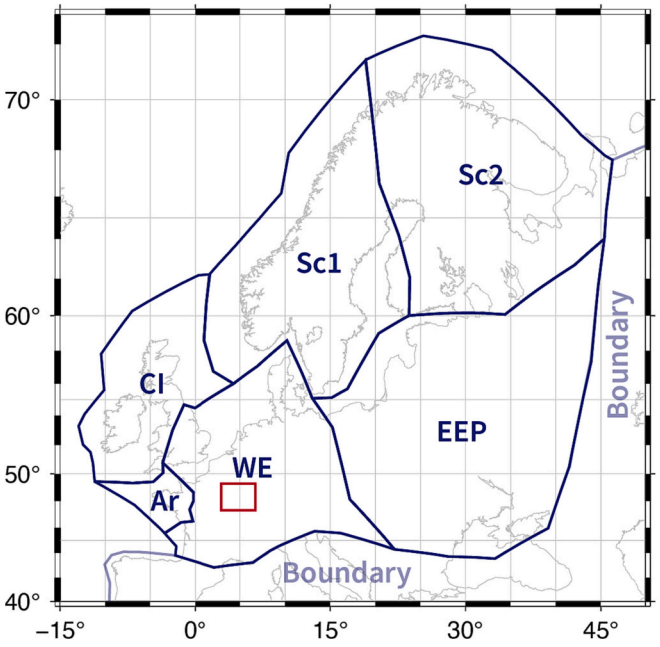

Fig. 3. Domains of assumed homogeneous lithosphere properties. Red rectangle is the study zone. Ar: Armorica, CI: Celtic Isles, EEP: Eastern European Platform, Sc1 and Sc2: Scandinavia, WE: Western Europe. (For interpretation of the references to colour in this figure legend, the reader is referred to the web version of this article.)

Table 1
Thermal, structural, and strain rate parameters of the domains. Sources: (1) ICONS (2022), (2) Baykiev et al. (2018), (3) Tesauro et al. (2008), (4) Chamorro et al. (2014), (5) Lucazeau and Vasseur (1989), (6) Majorowicz and Wybraniec (2011), (7) Majorowicz et al. (2019), (8) Veikkolainen et al. (2017), (9) Nurmi and Oy (2021), (10) Masson (2019), (11) EPOS (2022), (12) Tesauro et al. (2009b), (13) Cloetingh et al. (2007), (14) Artemieva et al. (2006).

Parameter	Lithospheric domain						Sources
	Ar	EEP	CI	Sc1	Sc2	WE	
Sediment thickness (km)	0	0–2	0–1	0		0–3	(1) (2)
Crustal thickness (km)	30–35	40–55	23–37	32–47	40–62	25–35	(2) (3)
Surface heat flow (mW.m^{-2})	40–100	40–60	40–85	30–60	20–60	65–110	(2) (4) (5) (6) (7) (8) (9)
Strain rate (GNSS) (s^{-1})	1.59×10^{-17}	1.64×10^{-17}	5.08×10^{-16}	2.2×10^{-16}		2×10^{-17}	(10) (11)
$z_{1200°C}$ (km)	140–170	140–220	130–160			100–160	(12) (13) (14)
$z_{1300°C}$ (km)				110–180	200–300		

- The Celtic Isles (CI) domain has a relatively thin crust (23–37 km), average surface heat flow (40–85 mw.m^{-2}), and intermediate GNSS-derived strain rates (5×10^{-16} s^{-1}).
- The Armorica (Ar) domain corresponds to a small heterogeneity in westernmost Europe in terms of surface heat flow (40–100 mW.m^{-2}), between those of the Celtic Isles and Western Europe.

Using these parameters, T_e values are computed for each domain (Fig. 4). Computation details are given in Section S1 of the supplementary material.

Our results (Fig. 4) illustrate the variability of T_e in the different domains. Three main points can be put forward:

- Overall, our T_e estimates are consistent with those in previous studies (Section S1.3 of the supplementary material).
- The T_e distributions are complex and multimodal. These distributions are tested in multiple T_e combinations (Sections S1.4 of the supplementary material). In the following, we retain the intermediate and extreme values, as they are representative of the combination range.
- Our results allow taking into account a larger range of potential T_e compared to previous studies (Section S1.3 of the supplementary material).

3.3.2. Atlantic Ocean T_e

We define oceanic T_e by its relation with oceanic lithosphere age and geotherm (Watts and Zhong, 2002). Observations of ocean lithosphere flexure related to its age suggest that T_e can globally be approximated by the depth of the 300–600 °C isotherms. For the Atlantic Ocean, this corresponds to T_e of 3–10 km at the mid-ocean ridge (age 0 Myr) and 20–40 km for the oldest parts of the lithosphere in the Gascogne gulf (age 80 Myr). An intermediate model assuming T_e to be related to the 450 °C isotherm depth suggests T_e values of 5 km by the ridge and 30 km in the Bay of Biscay. Overall, assumptions on Atlantic Ocean T_e have a very limited impact on our computations in the Paris Basin, due to the great distance to the ice loads and the study zone.

3.3.3. Elastic parameters and equivalent thickness (T_e) of the lithosphere

Elastic parameterization of the equivalent elastic plate representing the lithosphere rigidity is based on reference values from Turcotte and Schubert (2002) (Young's modulus of 10^{11} Pa and Poisson ratio of 0.25). We also consider a mean lithosphere density of 3000 kg.m^{-3}, as required in our finite elements Scandinavian and Celtic GIA models. We tested the impact of lateral T_e heterogeneities in our models by considering several value combinations between the different domains (Section S1.4 of the supplementary material). In order to simplify the analysis, we retain three T_e models representing minimum, intermediate, and maximum estimates (Fig. 5). Our tests indicate that these models are representative of the overall variability on T_e estimates, including those of other authors (Audet, 2014; Kaban et al., 2018; Tesauro et al., 2009a, 2012a, 2012b, 2013), and of the variability of the computed GIA stress perturbations in our study area (Section S1.4 of the supplementary material).

The range of our estimates can show very low values, as in the Scandinavian shield with T_e of 25–30 km. Such a low value is very unlikely for an Archean (3.2–2.5 Ga) to Phanerozoic (510–400 Ma) continental shield (Lahtinen et al., 2005) consisting of a thick and cold lithosphere (Artemieva et al., 2006; Artemieva, 2019; Cloetingh et al., 2007). In comparison, Tesauro et al. (2012a) find values >35 km in the Scandinavian shield, with a peak at 65–80 km. In the Alps, Tesauro et al.

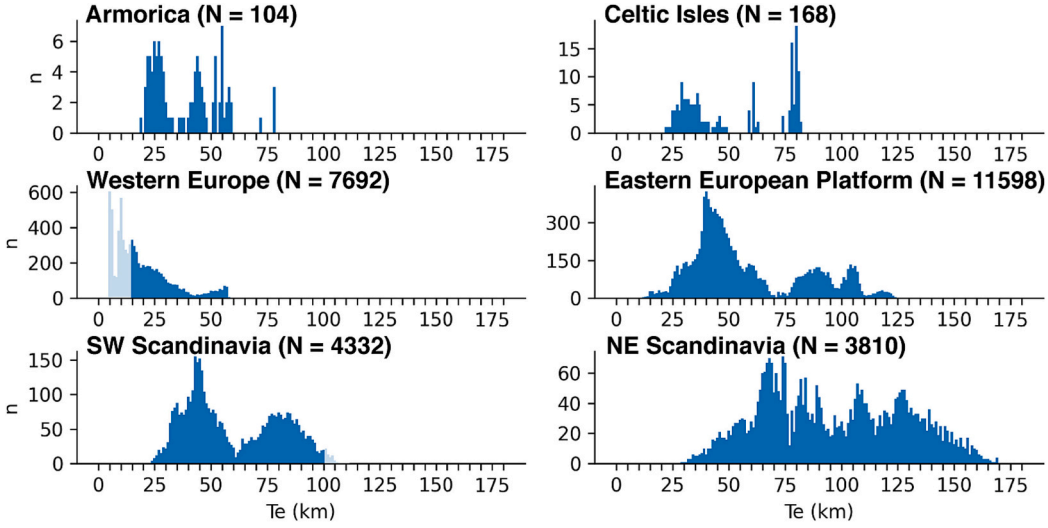

Fig. 4. T_e estimates for the European lithosphere domains. Light blue: estimates rejected based on the comparison with other studies (Audet, 2014; Kaban et al., 2018; Tesauro et al., 2009a, 2012a, 2012b, 2013).

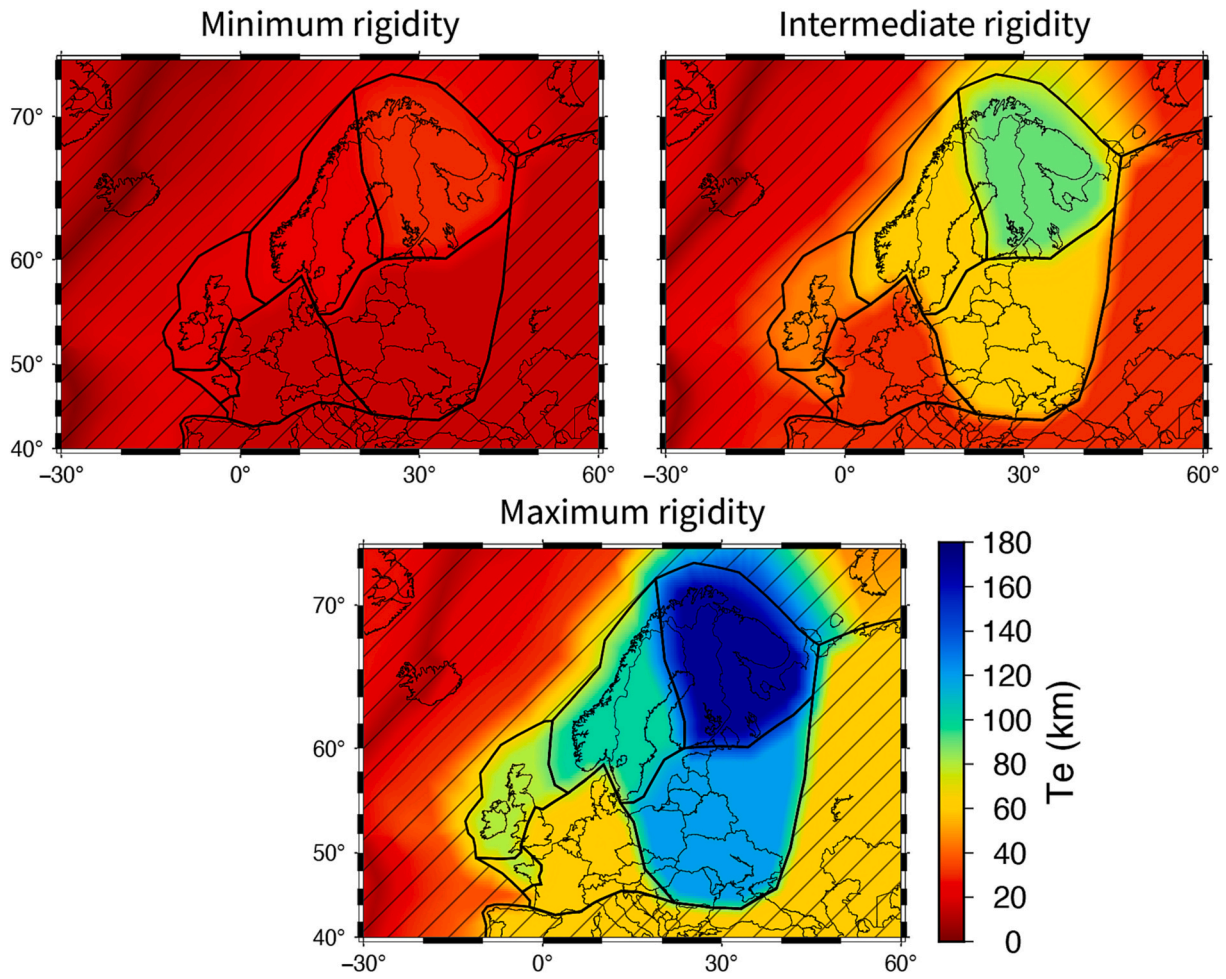

Fig. 5. Models of lithosphere equivalent elastic thickness (T_e) for GIA computation. T_e values in the hatched area have no impact on the computations in the study zone (Section S1.3 of the supplementary material).

(2012a) T_e range is 25–30 km, about twice the values we obtained for our minimum T_e model. While our minimum model provides T_e values that may be considered too low, the temperature profile associated with these lithosphere strength models is consistent with tomographic temperature estimates (Artemieva et al., 2006; Cloetingh et al., 2007; Tesauro et al., 2009b) and cannot be rejected. Our intermediate and maximum model values are more consistent with Tesauro et al. (2012a) estimates for Western Europe, including the Scandinavian shield. Thus, we consider our minimum model as an extreme case that must be retained to cover the full range possibilities, but we point out that the intermediate and maximum models are the most likely to represent actual lithosphere rigidity.

3.4. Mantle viscosity

We use two mantle viscosity models in our GIA computations. For the Alpine and Massif Central GIA models, we assume a simple exponential decay that represents the viscous relaxation of the mantle after the ice load melted. For the Scandinavian and Celtic GIA models, we use a layered mantle viscosity model. In both cases, we assume a laterally homogeneous viscosity structure. The combination of these two approaches is warranted by the similar magnitudes of the viscosity in both cases.

3.4.1. Scandinavian and Celtic GIA

Our mantle viscosity model for the Scandinavian and Celtic GIA computation is based on the values proposed by Lambeck et al. (2017) (5.1×10^{20} Pa s for the upper mantle and 1.3×10^{22} Pa s for the lower mantle), determined by adjustment to relative sea level data. The viscoelasticity structure is based on the Preliminary Reference Earth Model (Dziewonski and Anderson, 1981). Steffen and Kaufmann (2005) propose similar mantle viscosity values beneath northern Europe (Scandinavia, Barents Sea, Celtic Isles): 4–7 $\times$ 10^{20} Pa s for the upper mantle and 10^{22}–10^{23} Pa s for the lower mantle, according to paleo-shoreline data. Parametric tests in this study indicate that the lower mantle viscosity is not well constrained and may vary between 10^{22} and 10^{23} Pa s. Because of the different T_e values used in our models, we adjust the upper and lower mantle viscosities to 4–5 $\times$ 10^{20} Pa s and 1.3 $\times$ 10^{22} Pa s, respectively, in order to obtain present-day vertical velocities in Scandinavia consistent with GNSS data (Section S2.1 of the supplementary material). Parameters used in our Scandinavian and Celtic GIA computations are given in Table 2.

3.4.2. Alps and Massif Central GIA

Due to the relatively small spatial extent (100–250 km) and thicknesses (few hundred meters) of the ice loads, GIA interaction with the mantle is limited to the upper 100–200 km of the asthenosphere viscosity structure (see supplementary Section S2.2). The response of the lithosphere and upper asthenosphere can be approximated by that of an elastic plate over an isoviscous fluid, neglecting the effect of the complex upper and lower mantle viscosity structure.

In our models, the mantle relaxation is defined by a characteristic time of 7–8 kyr. These values are defined by adjusting the present-day predicted uplift rates to GNSS uplift velocities, assuming that the

Table 2
Layered Earth model parameters for Scandinavian and Celtic GIA computations.

Layer	Depth (km)	Density ρ (kg.m^{-3})	Poisson ratio ν	Young's modulus E (Gpa)	Viscosity μ (Pa s)
Elastic lithosphere	T_e (Section 3.3.3)				
Upper mantle 1	410	3433		182	$4–5 \times 10^{20}$
Upper mantle 2	670	3837	0.3	263	
Lower mantle	2800	4853		552	1.3×10^{22}

measured GNSS uplift signal in the Alps is mostly related to postglacial isostatic readjustment (Section S2.2 of the supplementary material). Eq. (7) relates the linear mantle viscosity (μ) to its characteristic time (τ) and the spatial wavelength of a considered load (λ) (Turcotte and Schubert, 2002):

$$\mu = \frac{\tau \rho g \lambda}{4\pi} \tag{7}$$

with ρ the mantle density and g the gravitational acceleration. For τ = 7–8 kyr and λ = 150–250 km (Alpine ice load width), the upper mantle viscosity is about 0.8–1.5 $\times$ 10^{20} Pa s. This is similar to the estimation of 1.4–2.8 $\times$ 10^{20} Pa s from Mey et al. (2016), who consider a slightly larger spatial wavelength of the ice load.

4. GIA stress perturbations

4.1. Computed flexure and stress perturbations fields

The combined flexure and stress perturbations due to the Alpine, Massif Central, Scandinavian, and Celtic ice loads at the LGM (21 ka) are shown in Fig. 6. In this section, the stress perturbations are considered alone and must be taken as an increase or decrease of ambient stresses

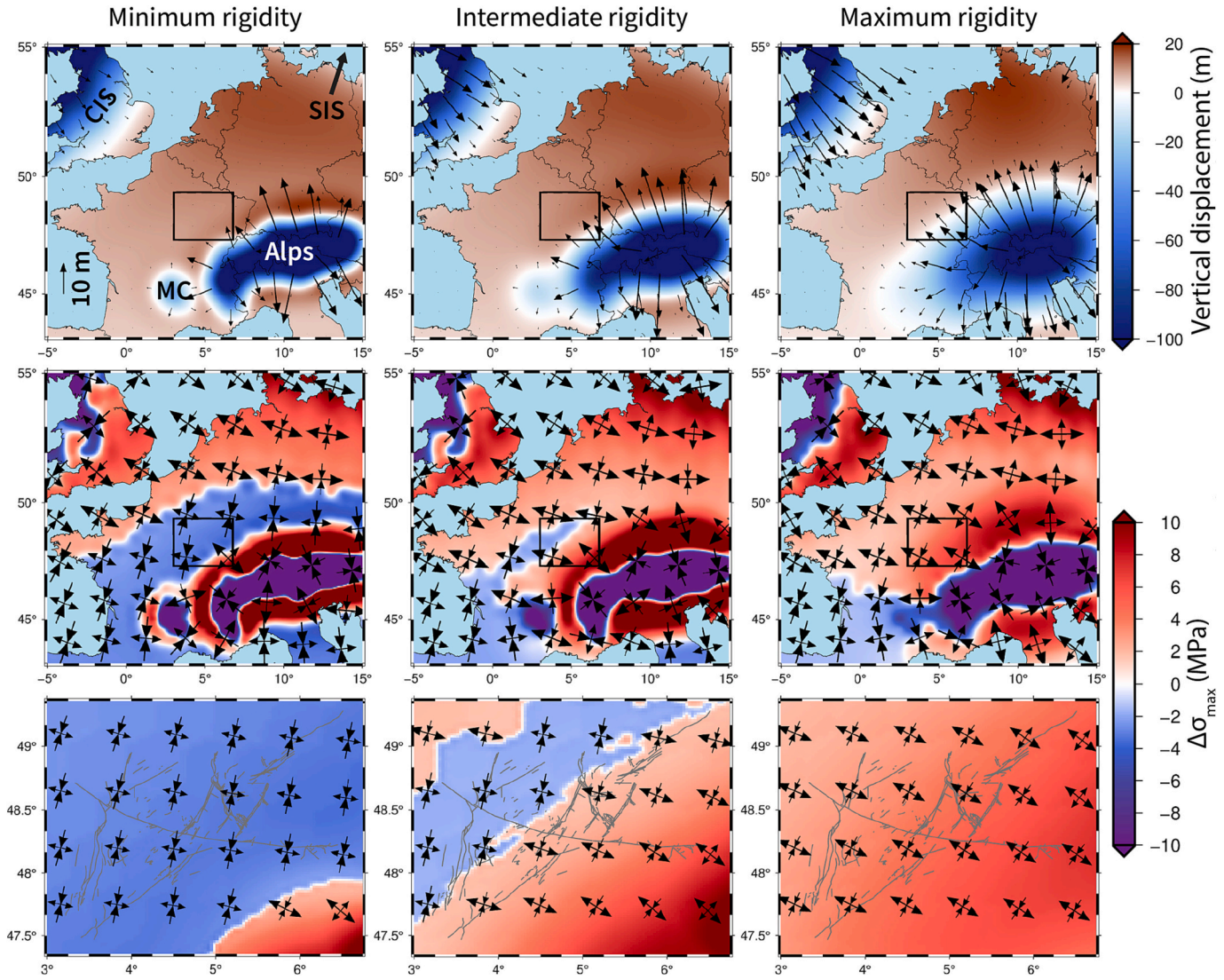

Fig. 6. LGM-state (21 ka) flexure and stress perturbation fields. Upper row: vertical (colormap) and horizontal (vectors) displacements of Earth surface (compared to an undeformed planar state). Middle row: horizontal stress perturbations over western Europe; lower row: horizontal stress perturbations in the study zone (black rectangle in upper and middle rows). The last two rows show horizontal stress perturbation tensors (crosses) and maximum horizontal stress perturbation (colormap): $\Delta\sigma_{max} = max(\Delta\sigma_1, \Delta\sigma_2, \Delta\sigma_1 + \Delta\sigma_2)$, with σ_1 and σ_2 the principal stresses. Positive and negative $\Delta\sigma_{max}$ values indicate tensile and compressive stresses, respectively. Gray lines on the lower row are known faults in the eastern Paris Basin.

(cf. Section 5). In the eastern Paris Basin, the effect of the Massif Central glaciers is negligible. The effects of the Alpine, Scandinavian, and Celtic ice loads interplay and their combination results in N-S compression or NW-SE tension in the study area depending on the T_e model. For the minimum lithosphere rigidity model, N-S compression dominates in the study zone, associated with the outer flank of the Scandinavian and Celtic forebulges. In contrast, the maximum rigidity model is associated with NW-SE tension in the whole study zone due to the combination of tensile stresses in the Alpine, Scandinavian and Celtic forebulges. In the intermediate lithosphere rigidity model, the eastern Paris Basin corresponds to the area of transition between compressional and tensile effects (Alpine NW-SE tension to the south, Scandinavian N-S compression to the south, Fig. 6). In all cases, GIA stress perturbations in the study area range between 2 and 7 MPa.

In contrast, present-day-state results in the study zone are homogeneous regardless of the T_e model and are primarily associated with far-field Scandinavian GIA. The computed stress perturbations show a N-S tension of 1–3 MPa (Fig. 7). The minimum rigidity model features minor *E*-W tension over the whole study area, while the intermediate and maximum rigidity model feature a mix of minor E-W compression and tension. As expected, the more rigid the lithosphere, the smaller the amplitude of the Scandinavian and Celtic GIA stress perturbations.

4.2. Coulomb failure stress perturbation

We estimate the far-field GIA impact on fault stability by calculating the Coulomb Failure Stress perturbations (ΔCFS):

$$\Delta CFS = \Delta\tau - \mu \times \Delta\sigma_n \tag{8}$$

with μ the fault friction coefficient, $\Delta\tau$ the fault-tangential stress perturbation (in the rake direction), and $\Delta\sigma_n$ the fault-normal stress perturbation, resolved on a given fault geometry. This criterion indicates the tendency of GIA to bring a given fault closer to failure (positive value) or rather to inhibit its failure (negative value). We assume a friction coefficient of 0.6 as a reference value (Byerlee, 1978) and test fault azimuth and dip angle between 0 and 360°N and 60–90° dip, respectively. This analysis is done for 5 sites chosen to cover the eastern Paris Basin fault network (Fig. 8) and to estimate ΔCFS variability in our study area. Tests with a low fault friction ($\mu = 0.1$) show similar results

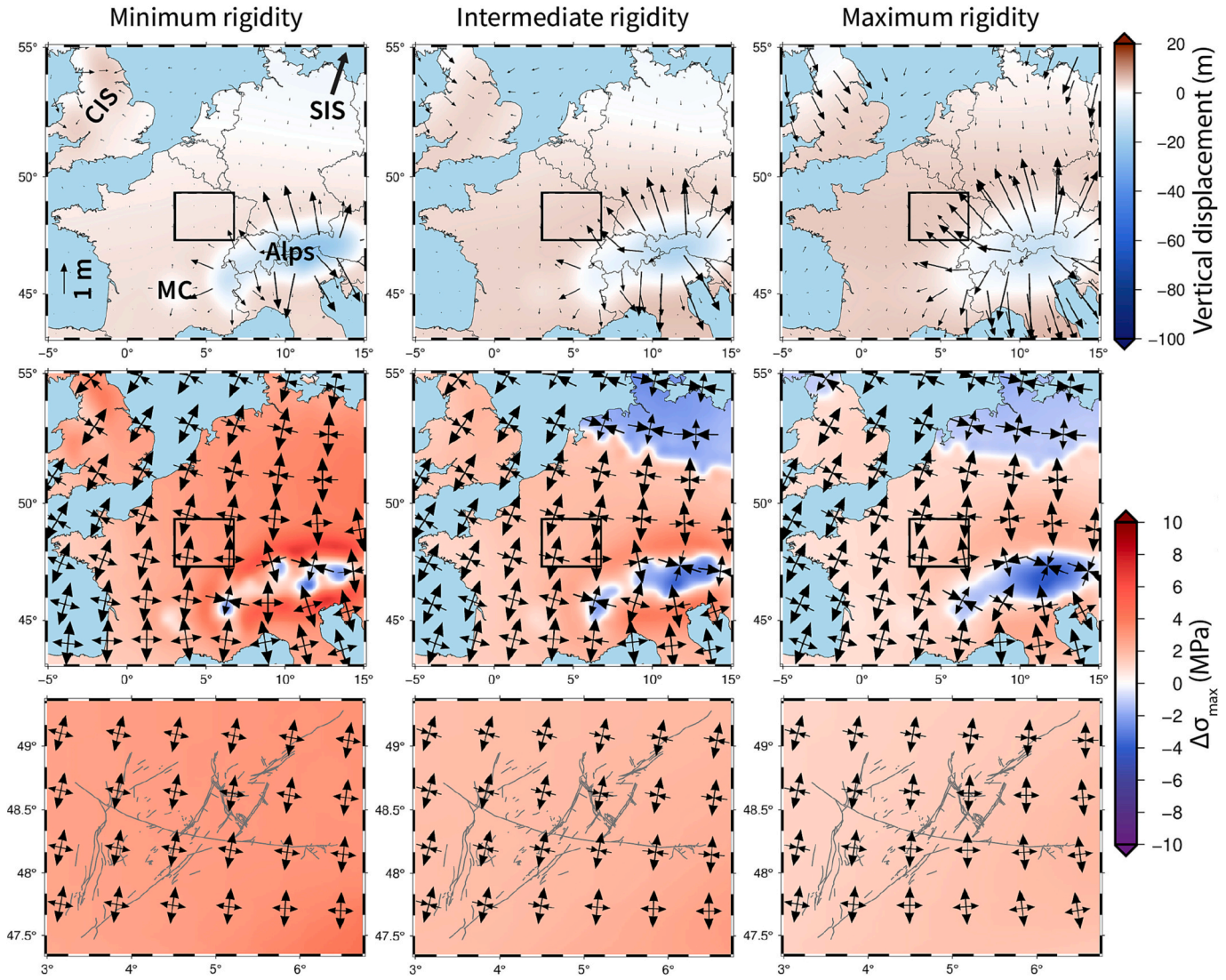

Fig. 7. Present-day-state flexure and stress perturbation fields. Upper row: vertical (colormap) and horizontal (vectors) displacements of Earth surface (compared to an undeformed planar state). The horizontal displacement vector scale is different from the one in Fig. 6. Middle row: horizontal stress perturbations over western Europe; lower row: horizontal stress perturbations in the study zone (black rectangle in upper and middle rows). The last two rows show horizontal stress perturbation tensors (crosses) and maximum horizontal stress perturbation (colormap): $\Delta\sigma_{max} = max(\Delta\sigma_1, \Delta\sigma_2, \Delta\sigma_1 + \Delta\sigma_2)$, with σ_1 and σ_2 the principal stresses. Positive and negative $\Delta\sigma_{max}$ values indicate tensile and compressive stresses, respectively. Gray lines on the lower row are known faults in the eastern Paris Basin.

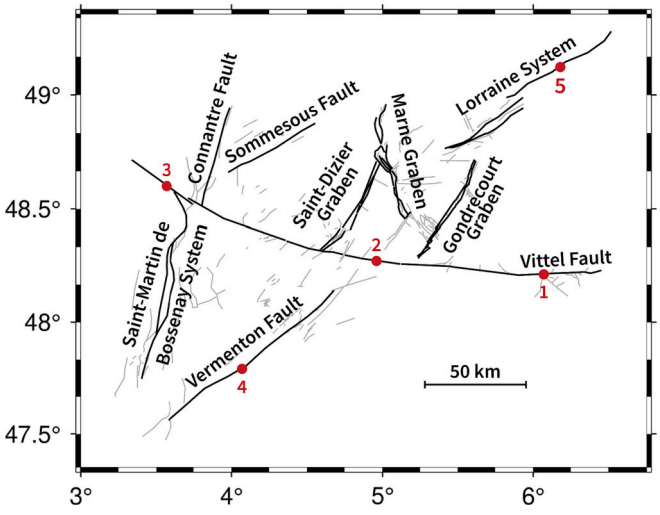

Fig. 8. Investigation sites for ΔCFS computation (numbered red dots) and major fault structures of the eastern Paris Basin. (For interpretation of the references to colour in this figure legend, the reader is referred to the web version of this article.)

to those with a standard friction, with minor variations of at most 1 MPa in the ΔCFS values.

At the LGM state, most fault geometries show positive ΔCFS values between 1 and 8 MPa, indicating a tendency of GIA to destabilize faults while the ice loads are in place (Fig. 9). Negative ΔCFS values between −0.1 and − 1 MPa are computed for very limited ESE-WNW geometries. This corresponds to the combined effect of N-S compression and NE-SW tension (Fig. 6).

At present-day state, the amplitudes of the Alpine stress perturbations are close to 0 MPa in the study area, so ΔCFS are mostly due to tensile stress perturbations associated with the Scandinavian and Celtic GIA. This results in quasi-exclusively positive ΔCFS for nearly all fault orientations and dips (Fig. 10), in contrast with the LGM state results. Present-day-state positive ΔCFS are between 0.8 and 2 MPa.

These positive ΔCFS values indicate that stress perturbations due to the combined effects of far-field Alpine, Celtic, and Scandinavian GIA tend to promote fault instability in the eastern Paris Basin throughout the glaciation period, up to present-day. The computed GIA effects result in long-wavelength homogeneous stress perturbation patterns, their impact is similar over our study but also in all northern France and neighboring regions away from the ice loads (Figs. 6 and 7).

5. Fault stability in combined GIA and regional stress fields

In order to estimate fault stability in the eastern Paris Basin, we apply the computed GIA stress perturbations to various ambient stress field models. Hereafter, fault stability is expressed by the Coulomb Failure Stress (CFS), with positive and negative values indicating fault instability (possible slip) and stability (impossible slip), respectively:

$$CFS = \tau - \mu\sigma_n \tag{9}$$

with τ the fault-tangential stress, μ the fault friction (fixed to 0.6 as a reference value, Byerlee, 1978), and σ_n the normal fault stress. We compute CFS for the same fault geometries as for ΔCFS (Section 4).

5.1. Ambient stress field modeling

We model a set of possible regional 3D crustal stress fields based on four constraints:

1) As shown by global borehole stress data, the upper crust is assumed to be critically stressed for failure on preferentially oriented faults with an effective friction of 0.6 (Brudy et al., 1997; Townend and Zoback, 2000; Zoback and Healy, 1992).

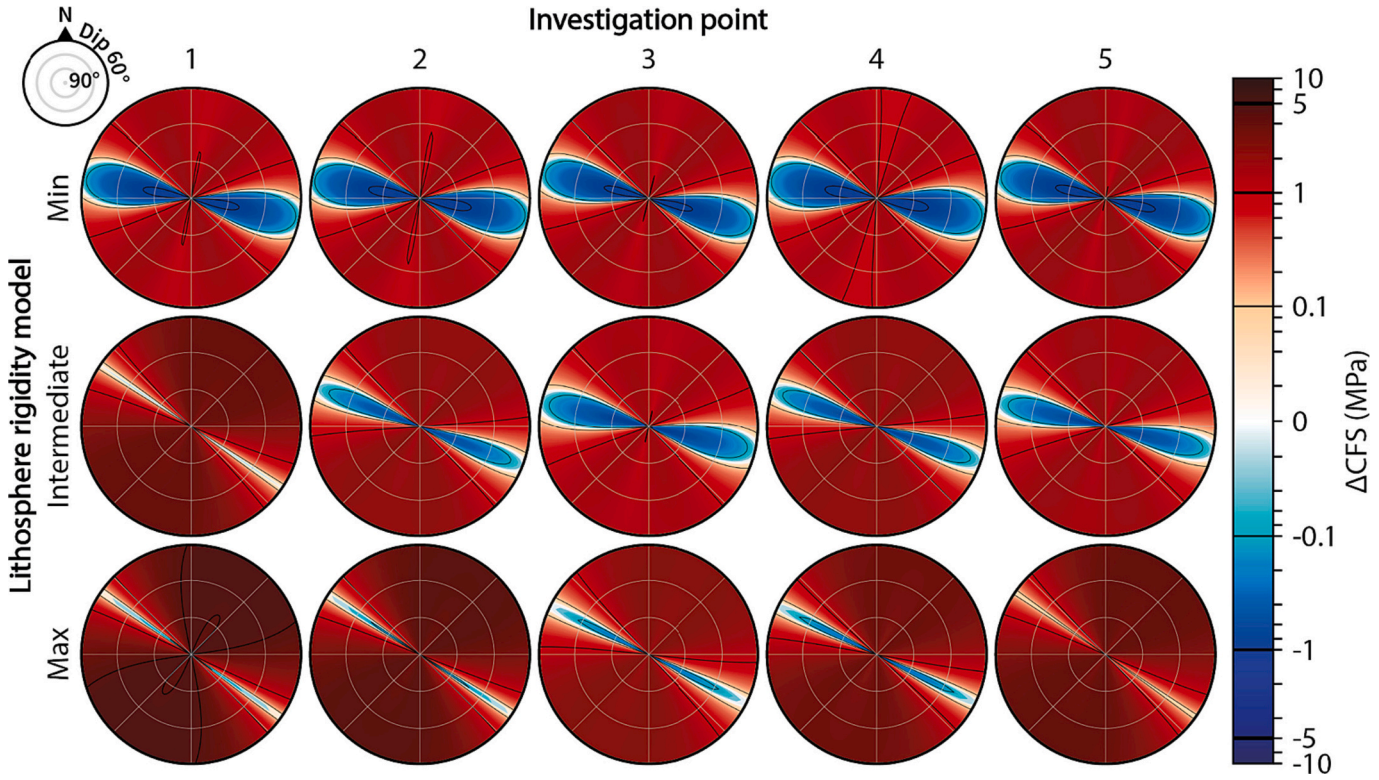

Fig. 9. LGM-state (21 ka) Coulomb Failure Stress perturbations. ΔCFS values are shown as a function of fault azimuth (North at the top of each graph) and dip (circle border = 60°, circle center = 90°). ΔCFS values of 0.1, 1, and 5 MPa are contoured (black lines).

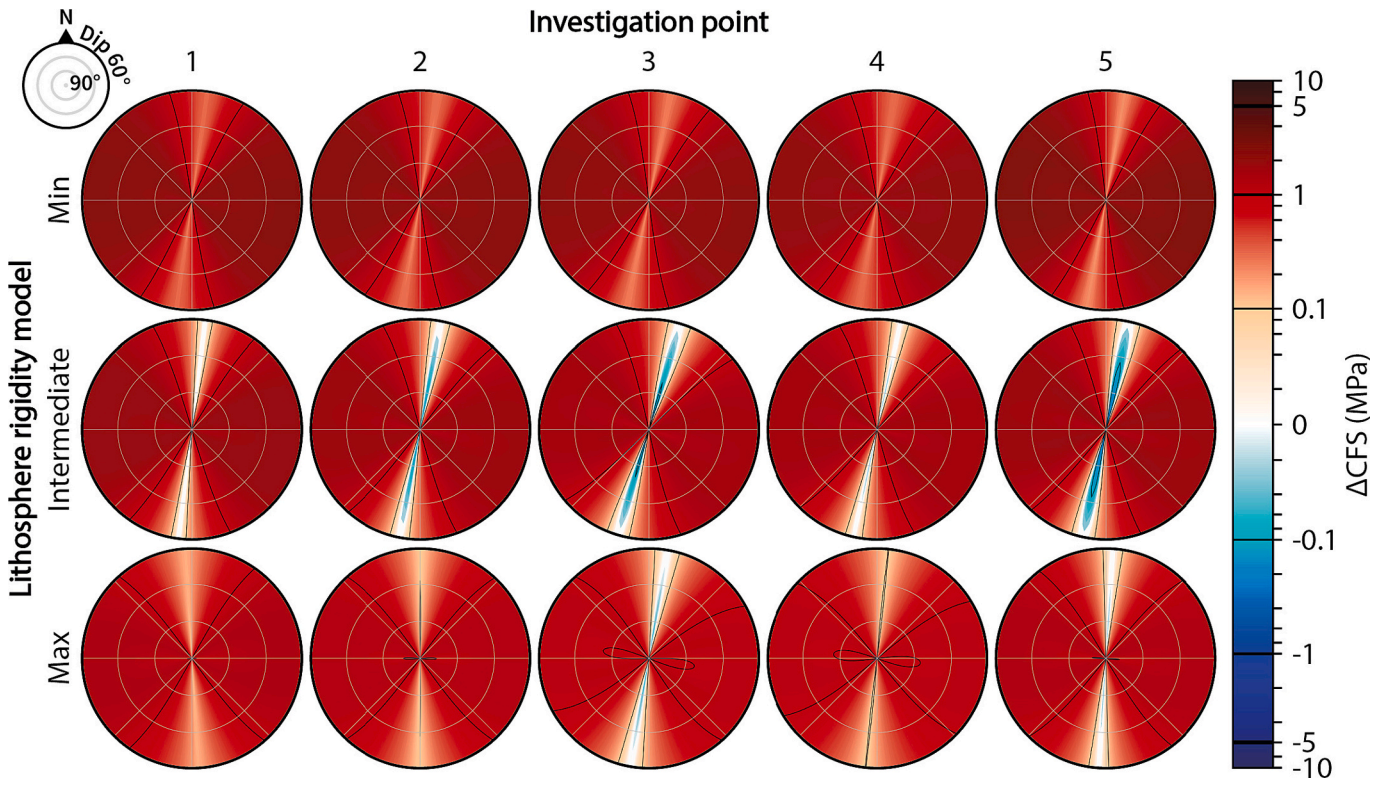

Fig. 10. Present-day-state Coulomb Failure Stress perturbations. ΔCFS values are shown as a function of fault azimuth (North at the top of each graph) and dip (circle border = 60°, circle center = 90°). ΔCFS values of 0.1, 1, and 5 MPa are contoured (black lines).

2) The regional stress field is associated with normal or strike-slip deformation regimes, as indicated by focal mechanisms around the study zone (Fig. 11) (Mazzotti et al., 2021).
3) The shape of the stress tensor is tested for three cases of the stress ratio R:

$$R = \frac{\sigma_2 - \sigma_3}{\sigma_1 - \sigma_3} \tag{10}$$

with σ_1, σ_2, and σ_3 the stress tensor principal components and R assumed to be 0.5, 0.75 or 1 (Fig. 12).
4) The principal stress components are oriented vertically and horizontally, with a maximum horizontal stress azimuth of 150°N as observed by borehole stress measurements in the eastern Paris Basin and nearby regions (Fig. 13) (André et al., 2006; Heidbach et al., 2016; Mazzotti et al., 2021; Wileveau et al., 2007).

Each of these possible regional stress fields are associated with specific fault geometries in a critical near-failure state (CFS = 0), without any GIA-induced stress perturbation. These correspond to Andersonian geometries in the considered ambient stress field (Anderson, 1905), with fault orientations at ±60° of the minimum stress (σ_3), parallel to the intermediate stress (σ_2) and at ±30° of the maximum stress (σ_1)

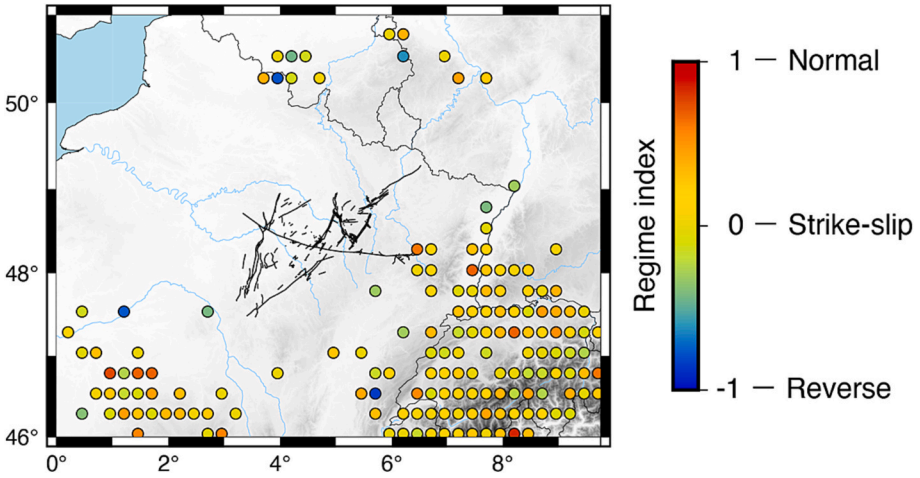

Fig. 11. Grid-average deformation regime around the study area, obtained from focal mechanisms (FMHex database, Mazzotti et al., 2021). Deformation regimes are averaged on a 25 × 25 km grid following: $\frac{\alpha_P - \alpha_T}{90}$, with α_P and α_T the mean dip angles of the compressional (P) and tensile (T) axes of the focal mechanisms within a 25 km square centered on each grid point.

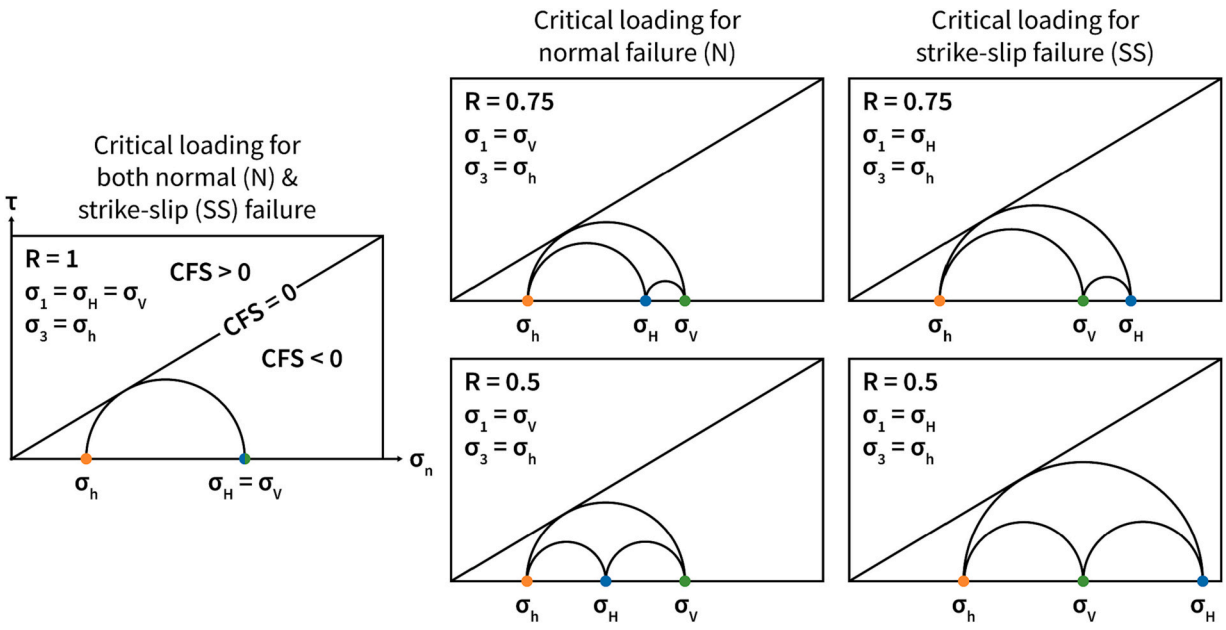

Fig. 12. Mohr circle schematic representations of regional critical stress fields. σ_H, σ_h, and σ_V are the maximum horizontal, minimum horizontal, and vertical stress, respectively.

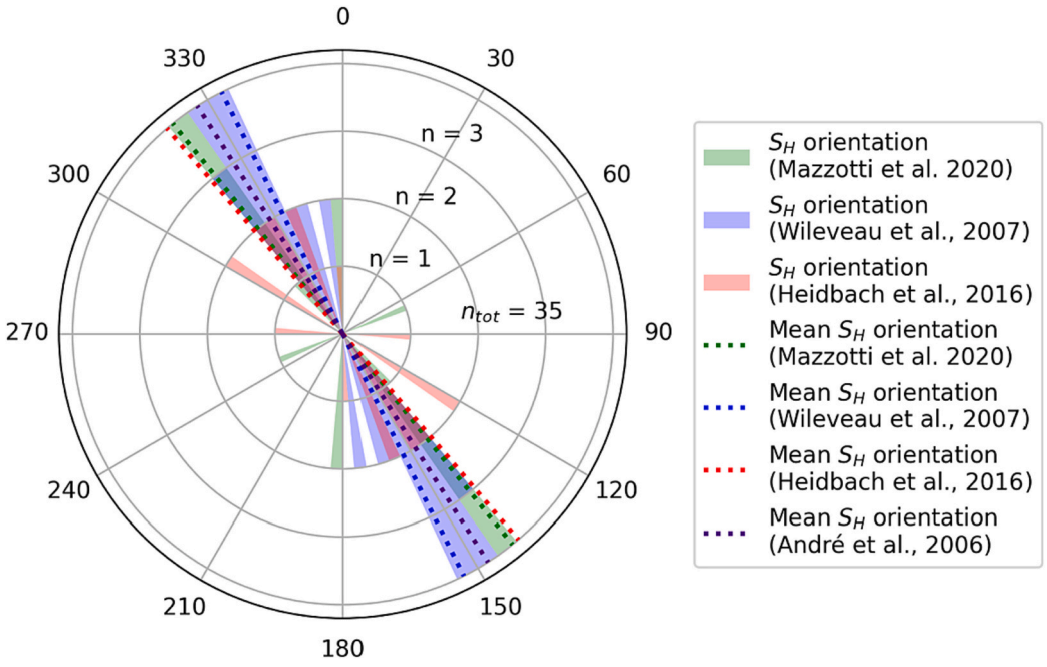

Fig. 13. Orientations of the maximum horizontal stress measured in the eastern Paris Basin.

(Fig. 14). In our cases, these correspond specifically to:

- In a normal-style stress field, faults parallel to the 150°N maximum horizontal stress (σ_2), dipping 60° (±30° from the vertical stress, σ_1).
- In a strike-slip-style stress field, vertical faults (90° dip, parallel to the vertical stress, σ_2) oriented at ±30° from the 150°N maximum horizontal stress (σ_1).

5.2. Fault stability in the Paris Basin

Because of the low variability in the GIA ΔCFS at the different investigation points (Figs. 9 and 10), in the following, we discuss the results at investigation point 2 (center of the fault network, Fig. 8), which is representative of the general tendencies for all points in the study area. This allows us to focus on discussing CFS as a function of the lithosphere rigidity and ambient stress models. In our ambient stress models, stresses range between 7 and 35 MPa at 1 km depth, increase to 40–190 MPa at 5 km depth and 85–400 MPa at 10 km depth. Given the relatively small amplitude of computed GIA stress perturbations compared to the ambient stresses, we consider that applying the GIA perturbations to ambient stress models at 1 km depth is representative of maximum GIA effect: GIA stresses are the largest at this shallow depth (top of the equivalent elastic plate) and of the same order of magnitude as the ambient stresses. Deeper fault sections are less sensitive to GIA

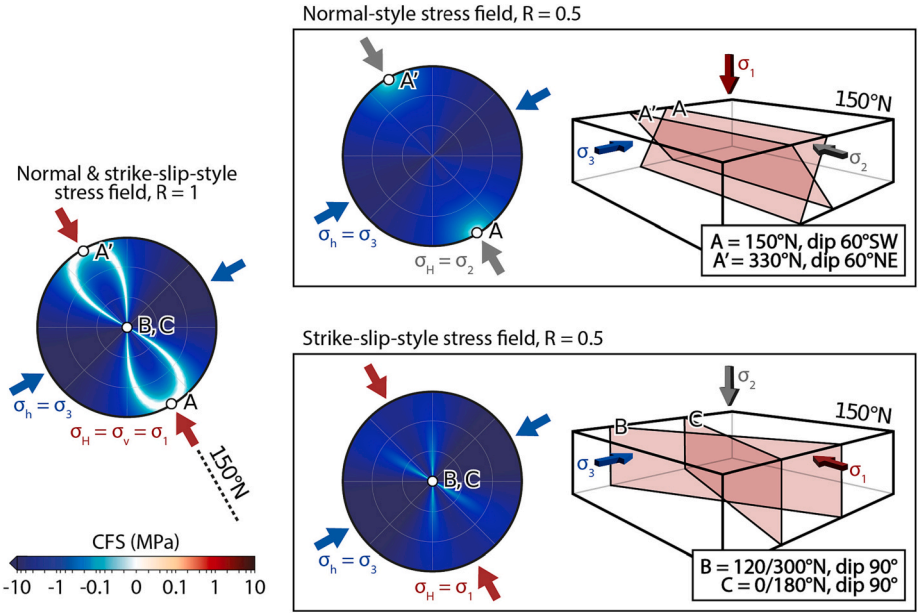

Fig. 14. Andersonian geometries for our regional stress field models. Stereograms: Coulomb Failure Stress on tested faults geometries (0–360°N, 60–90° dip) for our stress model end-members. A, B, and C correspond to the Andersonian fault geometries. 3D diagrams: representations of Andersonian fault geometries (A, B, and C) in relation with the principal stresses of the regional stress model.

perturbations as those diminish with depth and greater ambient stresses tend to clamp fault more efficiently. This 1 km depth is representative of the shallowest intraplate earthquakes (Schulte and Mooney, 2005) and allows considering the totality of the known eastern Paris Basin fault network. Working at greater depth would omit the impact of GIA on most of the faults in the eastern Paris Basin that are limited to the basin sedimentary cover (3 km at most, Fig. 1).

Overall, because the GIA stress perturbations are small compared to the ambient stresses, faults showing a potential instability (positive CFS) are those with a geometry close to the Andersonian model in the regional stress field (Fig. 14): 60° dipping normal faults oriented 150°N and vertical strike-slip faults oriented 120°N and 180°N (Figs. 15 and

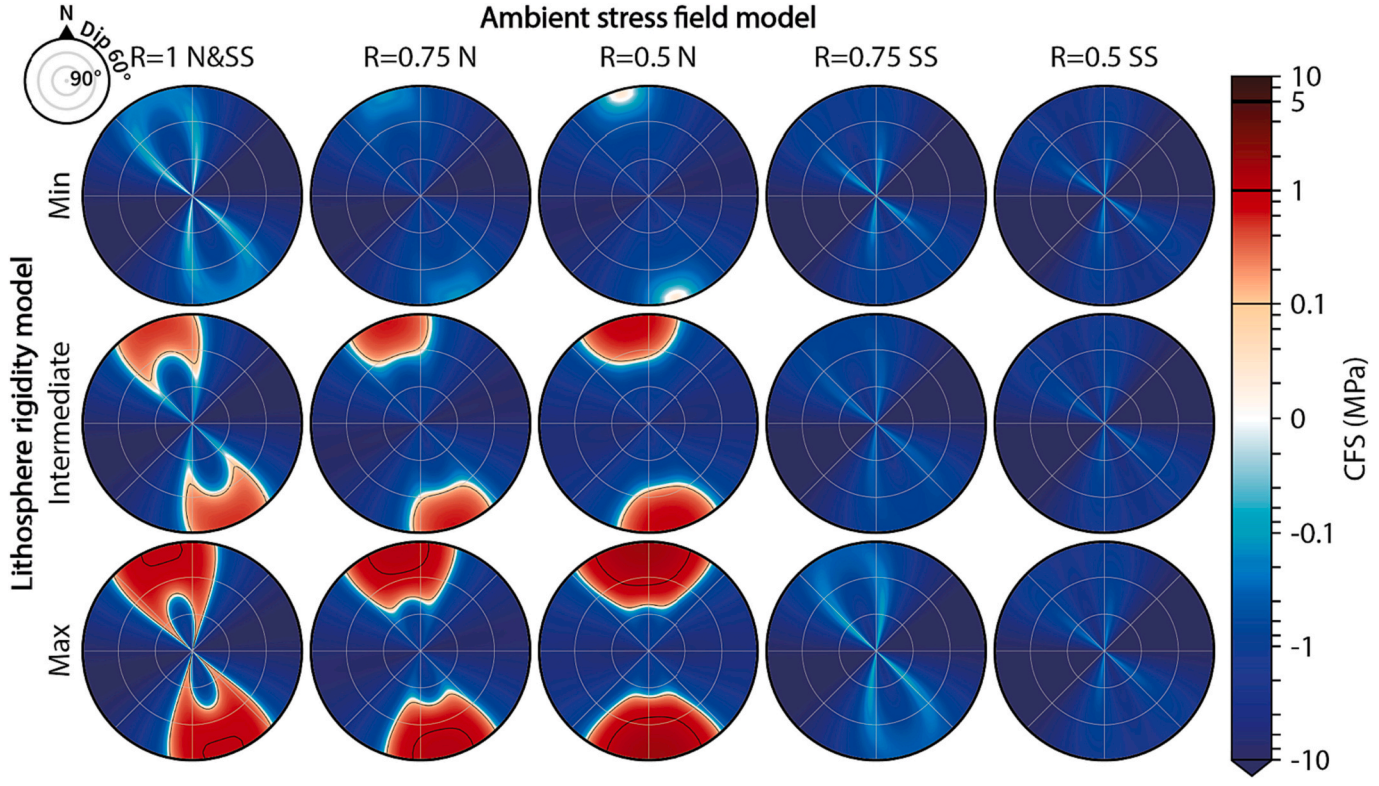

Fig. 15. LGM-state (21 ka) Coulomb Failure Stress as a function of lithosphere rigidity and ambient stress field models. R: stress ratio (cf. Section 5.1). N and SS: normal and strike-slip faulting styles. CFS values are shown as a function of the fault azimuth (North at the top of the graph) and dip (circle border = 60°, circle center = 90°). Positive CFS values of 0.1, 1, 5 MPa are contoured (black lines).

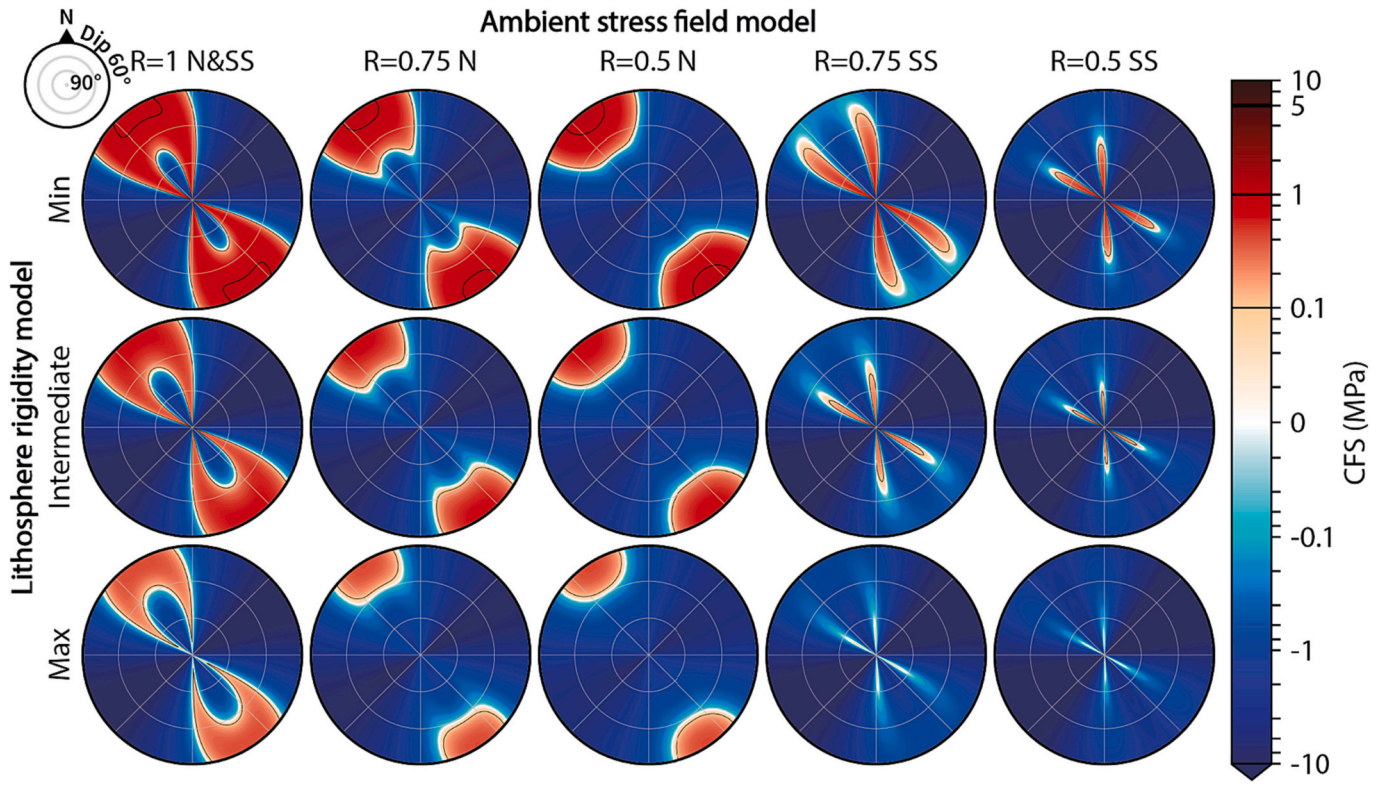

Fig. 16. Present-day-state Coulomb Failure Stress as a function of lithosphere rigidity and ambient stress field models. R: stress ratio (cf. Section 5.1). N and SS: normal and strike-slip faulting styles. CFS values are shown as a function of the fault azimuth (North at the top of the graph) and dip (circle border = 60°, circle center = 90°). Positive CFS values of 0.1, 1, 5 MPa are contoured (black lines).

16). However, the GIA stress perturbations at the LGM state expand the range of potentially unstable faults to those with azimuths of 130–220°N and dips of 60–80°, particularly for the maximum lithosphere rigidity model (Fig. 15). Overall, the main instability potential lies with 60–70° dipping faults in normal faulting regimes, with positive CFS values up to 1–2 MPa (Fig. 15). In contrast, GIA effects at present-day state result in a larger range of potential fault instability, with vertical strike-slip faulting on N-S and NW-SE faults, with positive CFS values up to 0.8 MPa, especially for the minimum lithosphere rigidity model. For the normal faulting style, the range of destabilized faults and positive CFS amplitude are reduced, compared to the LGM state, to ±20–30° of the Andersonian geometries and positive CFS values of 0.1–1 MPa (Fig. 16).

These estimations are made for an ambient stress at 1 km deep and assuming that the GIA perturbations are maximal (i.e., those at the top of the equivalent elastic plate). At greater depths (5–15 km), the relative amplitude of the GIA stress perturbations become smaller compared to the increasing ambient stresses. Even assuming the maximum GIA perturbations, our analyses show that, at 5–15 km depth, potentially unstable faults are much more restrained to Andersonian fault geometries (150 ± 5°N, 60–63° dipping normal faults and 120/180°N, 87–90° dipping strike-slip faults), compared to those at 1 km deep. The positive CFS values are limited to 1 MPa at most.

Based on these results, we conclude that far-field GIA effects can promote fault instability in the eastern Paris Basin from the LGM to present-day for well-oriented faults relative to the ambient stress field. Fig. 17 shows the resolution of CFS on the studied fault network for intermediate lithosphere rigidity scenario at LGM and present-day states. Well-oriented, potentially destabilized faults in the eastern Paris Basin correspond to the Marne, Connantre and Saint-Martin de Bossenay Fault systems, as well as the western end of the Vittel Fault system. These potentially unstable faults are oriented at less than ±35° relative to the ambient maximum horizontal stress. Other major faults in the Gondrecourt, Lorraine, Saint-Dizier, Sommesous, Vermenton, and Vittel systems are associated with negative CFS (i.e., GIA promotes fault stability).

Considering the steep 80° dip angle of the studied faults, present-day-state GIA stress perturbations result in greater positive CFS values than LGM-state ones (Fig. 17). Faults in the Saint-Martin de Bossenay and Western Vittel systems may thus show a greater reactivation potential at present-day-state than at LGM-state. Furthermore, faults in the Marne system show negative CFS values at LGM-state but positive CFS values at present-day state, indicating a transition from stable to unstable state between LGM and present-day.

6. Discussion

6.1. Dependence of the results on lithosphere rigidity, time, and depth

Our computations show a strong variability associated with lithosphere rigidity and timing in the glacial cycle. In a context of several GIA systems interacting in our study area, different stress perturbation regimes can be observed depending on the lithosphere rigidity (Fig. 6). Considering that GNSS vertical velocities in formerly glaciated areas are representative of postglacial uplift, we compare them to our models but find that they can all equally fit the GNSS velocities, preventing identifying an optimum lithosphere rigidity model. Hence, lithosphere rigidity configuration remains a major uncertainty and source of variability of our models.

The temporal evolution of the GIA effects results in style inversions and change in orientations of predicted stress perturbations (Figs. 6 and 7). To take into account the temporal evolution of the impact of GIA on fault stability, our models could be improved by using a finite-elements including explicit fault planes (e.g., Hampel et al., 2009; Steffen et al., 2014). Hampel et al. (2009), using a single ice load, show that fault activity out of the glaciated areas can occur during ice buildup, while our results for several ice loads lead to greater fault destabilization

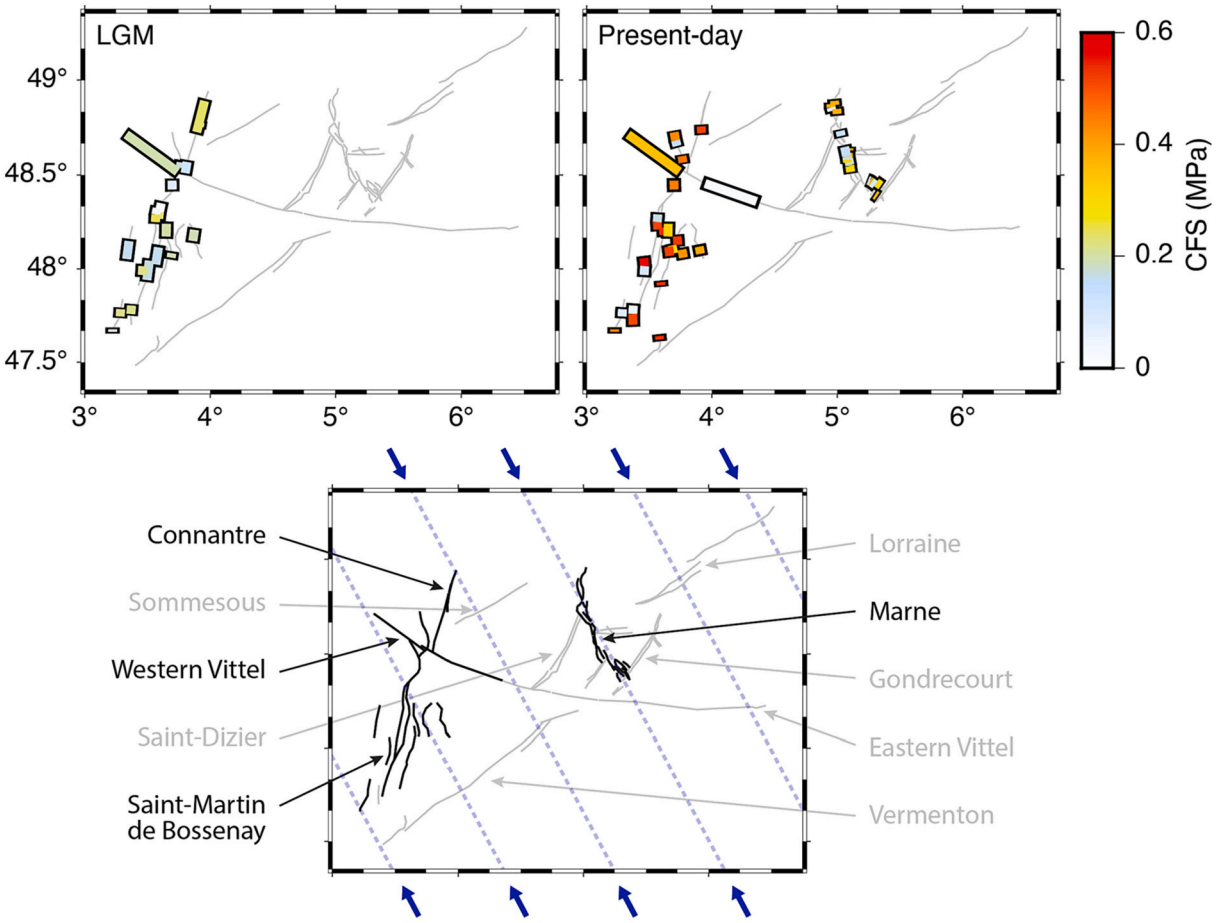

Fig. 17. Upper row: CFS values resolved on major fault planes of the studied network (only positive CFS are shown for clarity) for intermediate lithosphere rigidity and ambient stress model "$R = 1$, N&SS", at 1 km depth, for LGM and present-day states (left and right, respectively). Lower row: potentially unstable faults due to GIA effects at LGM or present-day states in the eastern Paris Basin (black lines). Gray lines: other known faults not destabilized by GIA. Blue dashed lines: regional maximum horizontal stress orientation. (For interpretation of the references to colour in this figure legend, the reader is referred to the web version of this article.)

during postglacial times for some of our GIA scenarios. This raises the question of the timing of the greatest glacially-induced fault destabilization in our study area: is it associated to a particular phase of the glacial cycle, or does it possibly occur in several episodes due to the complex interaction of the considered GIA systems?

Observations at the global scale indicating that the SCR earthquakes mostly locate in the upper third of the crust (Klose and Seeber, 2007). This supports our consideration of the computed stresses at the top of the elastic plate at 1 km depth to study the maximum effects of GIA on faults. This shallow depth is based on observations of shallow intraplate seismicity (Klose and Seeber, 2007; Schulte and Mooney, 2005), but one must keep in mind that the true depth at which elastic deformation affects the lithosphere remains unknown in our models.

6.2. *Consideration of more complex rheological features*

Our models do not consider a possible crustal viscosity layering, lateral heterogeneity in mantle viscosity, structural inheritance, or rheological heterogeneities in the sedimentary basin or the crust. Schotman et al. (2008) suggest that viscosity in the lower crust may have an impact on GIA computations resulting in a few meters in amplitude of the maximum lithosphere flexure, and a difference on the position of the forebulge of a few tens of kilometers. Di Donato et al. (2000) suggest that considering lower crust viscosity may help improve the fit of models to uplift rates by few tenths of mm/yr. Kaufmann and Amelung (2000) show that a low viscosity layer of 10^{18} Pa s in the uppermost mantle (30–200 km) allows a better agreement of model predictions with leveling data, but they also show that equivalent elastic thickness is as important as an eventual lower crust low viscosity layer for predicted lake-load-induced deformation to agree with leveling data. Hence, considering the variability of our primary rheological parameter T_e, the effects of lower crust viscosity are likely to be well covered by the overall variability of our models.

Our models do not include dynamic fault elements as used in Hampel et al. (2010) and Turpeinen et al. (2008). Including such features may allow to study the temporal variations of the predicted impact of GIA on fault stability, as well as the amplitude of this impact in terms of slip rates. Yet, models used by Hampel et al. (2010) and Turpeinen et al. (2008) require the implementation of poorly-constrained boundary condition velocities in order to initiate fault slip and study the impact of GIA on fault slip rates. Such velocities are difficult to constrain in our study area, which shows very small deformation rates, and would represent a large source of uncertainty. Our analysis of GIA impact on fault stability with a static CFS is free of this additional uncertainty. Yet, future works should focus on testing GIA modulation of fault slip rates for different boundary velocity configurations.

Other rheological features may induce more complex effects that our models do not take into account: lateral mantle viscosity heterogeneities may have a strong impact on GIA deformation (Bagge et al., 2021; Steffen et al., 2006; Van der Wal et al., 2013), structural inheritance along major tectonic structures may localize deformation and stresses induced by both long-term processes (Mazzotti and Gueydan, 2018; Tarayoun et al., 2019) and GIA (Tarayoun et al., 2018; Wu and Mazzotti, 2007). While broad rheological features of the Earth can be constrained

by relative sea-level and paleo-shoreline data (Tushingham and Peltier, 1992), geodetic velocities (Argus and Peltier, 2010), gravity rates (Lambert et al., 2001), and geodetic signals in areas showing large localized strain rates (Tarayoun et al., 2018), no such constraints exist in regions undergoing very small deformation far from the former ice systems, as in our study area. Thus, including these complexities in our models would result in adding variability that may extend the range of possible results.

6.3. Comparison to areas featuring potential glacially-induced fault activity

Few field studies in a context similar to the eastern Paris Basin report evidence of glaciotectonic activity in relation with the last glacial cycle allowing to discuss their timing (Brandes et al., 2012; Houtgast et al., 2005; Štěpančíková et al., 2022). Brandes et al. (2012) and Houtgast et al. (2005) find ages for deposited sediments near major faults in their study areas of 29–13 ka and 23–13.5 ka, respectively. Both cases feature deformation evidence that suggest tectonic activity contemporary or posterior to the deposition of the sediments. Štěpančíková et al. (2022) report fault activity offsetting of a 63–24 ka alluvial fan covered by undeformed sediments at 11 ka, suggesting fault movement during the 24–11 ka period. These three studies point to glaciotectonic activity during the pleniglacial to postglacial times of the last glacial cycle, suggesting that GIA could have triggered this deformation. This is consistent with our results suggesting a greater destabilization potential in postglacial times rather than in pleniglacial times (Figs. 15, 16, and 17). Yet, this timing of maximum destabilization potential is contradictory with the results of Hampel et al. (2009), who suggest that fault activity out of the glaciated areas occurs during the ice buildup phase. This difference in timing of the maximum fault destabilization potential could possibly denote the impact of the interplay between several ice systems.

6.4. Main conclusions and comparison to northern France seismicity

We show that, compared to ambient stresses that are the major control on fault stability, glacially-induced stresses are small. Yet, for specific fault geometries that are well oriented, glacially-induced stresses can be large enough to lead to fault destabilization (Figs. 15 and 16). The stress perturbation amplitudes are similar to coseismic stress drop (Courboulex et al., 2016) and stress perturbations associated with known fault activation (Stein et al., 1992; Zhang et al., 2008). Well-oriented fault geometries exist in the eastern Paris Basin, corresponding to ~120/180°N, 80° dipping faults (mean dip angle of the studied faults) mainly located in the Marne and Saint-Martin-de-Bossenay systems (Fig. 17), but without reported activity for the last 15 Ma.

Because both the ambient stress field (Heidbach et al., 2016; Mazzotti et al., 2021; Mazzotti et al., 2020) and the present-day GIA stress perturbations are similar for most of the Paris Basin and northern France, our local analysis may be extended to seismically active regions of northern France for comparison. Fig. 18 shows a subset of large-scale crustal faults (BDFA database, IRSN, 2022) that may fall within the range of potential instability in response to the combined far-field Alpine, Massif Central, Scandinavian and Celtic GIA stress perturbations. Potentially unstable faults in the Armorican Massif and Rhine Graben are located in seismically active regions, while other potential unstable faults are located in the seismically quiet Paris Basin, as shown by instrumental earthquake density. These variations in seismicity over hundreds of kilometers cannot be associated with GIA or regional stress heterogeneity, thus pointing to other processes that must play a role in the control of seismic activity.

7. Conclusions

Our modeling of Alpine, Massif Central, Scandinavian, and Celtic GIA shows that this process can induce stress perturbations of significant amplitude (ΔCFS = 1–8 MPa at LGM state, 0.8–2 MPa at present-day state) for fault reactivation at hundreds (200–750 km) of kilometers away from the ice systems. We show that, away from the ice systems, interactions of GIA effects from several ice centers result in stress combinations that depend on lithosphere rigidity and its lateral variations. The impact on fault stability varies through time in a different way than previously proposed by models considering a single ice load, with a

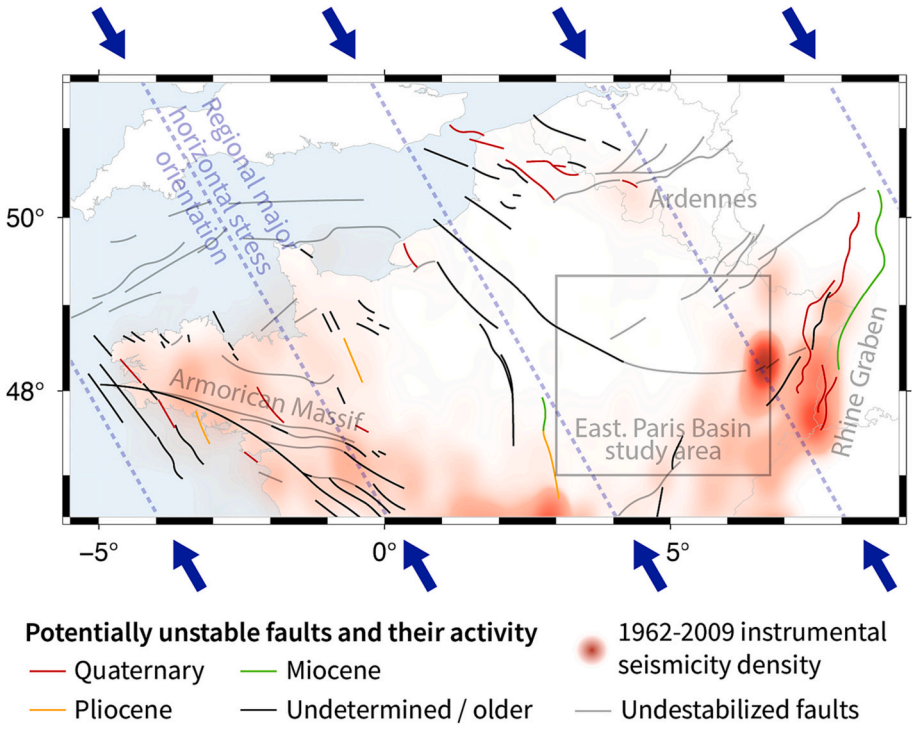

Fig. 18. Known faults close to Andersonian geometries that may be unstable due to GIA effects, timing of their last known activity (black and colored lines, BDFA database, IRSN (2022)), and density of instrumental earthquakes during 1962–2009 (SI-Hex database, Cara et al. (2015), red heatmap). Gray lines: other known faults that are not destabilized by GIA effects. Blue dashed lines: orientation of the maximum horizontal regional stress. (For interpretation of the references to colour in this figure legend, the reader is referred to the web version of this article.)

greater destabilization in the eastern Paris Basin during postglacial times than during pleniglacial times. The computed GIA stress perturbations are low compared to ambient crustal stresses, but they are sufficient to potentially destabilize faults close to Andersonian geometries (±10–30°). Such geometries are known in the eastern Paris Basin, corresponding to ~120 to 180°N, 80° dipping faults mainly located in the Connantre, Saint-Martin-de-Bossenay and Marne Fault systems, as well as the western end of the Vittel Fault system.

CRediT authorship contribution statement

Adrien Damon: Writing – review & editing, Writing – original draft, Visualization, Software, Resources, Project administration, Methodology, Investigation, Formal analysis, Data curation, Conceptualization. **Stéphane Mazzotti:** Writing – review & editing, Supervision, Project administration, Methodology, Investigation, Funding acquisition, Conceptualization. **Philippe Vernant:** Writing – review & editing, Supervision, Methodology, Investigation, Conceptualization. **Rémi Vachon:** Writing – review & editing, Software, Methodology, Investigation, Conceptualization. **Juliette Grosset:** Methodology. **Frédéric Ego:** Writing – review & editing, Supervision, Resources, Funding acquisition, Conceptualization. **David Baumont:** Writing – review & editing, Supervision, Conceptualization.

Declaration of Competing Interest

The authors declare the following financial interests/personal relationships which may be considered as potential competing interests:

Adrien Damon reports financial support was provided by ANDRA. Adrien Damon reports a relationship with ANDRA that includes: employment and funding grants.

Data availability

Data will be made available on request.

Acknowledgements

The GIA computation over Northern Europe was supported by the SEAMSTRESS project through the Tromso research foundation. It is also supported by the Research Council of Norway (grant 287865) and its Centers of Excellence funding scheme, project 223259.

Appendix A. Supplementary data

Supplementary data to this article can be found online at https://doi.org/10.1016/j.tecto.2023.230035.

References

Adams, J., Wetmiller, R.J., Hasegawa, H.S., Drysdale, J., 1991. The first surface faulting from a historical intraplate earthquake in North America. Nature 352, 617–619. https://doi.org/10.1038/352617a0.

Amelung, F., Wolf, D., 1994. Viscoelastic Perturbations of the Earth: Significance of the Incremental Gravitational Force in Models of Glacial Isostasy. https://doi.org/10.1111/J.1365-246X.1994.TB02476.X.

Ancrenaz, A., Define, E., Poiraud, A., 2020. Fluctuations glaciaires au Pléistocène supérieur dans les Monts d'Aubrac (Massif central, France): nouvelles données. Géomorphol.: Relief Process. Environ. 26 https://doi.org/10.4000/geomorphologie.14516.

Anderson, E.M., 1905. The dynamics of faulting. TRNED 8, 387–402. https://doi.org/10.1144/transed.8.3.387.

André, G., Proudhon, B., Rebours, H., Wileveau, Y., 2006. Paramètres contrôlant la distribution de la fracturation: exemple dans une série marno-calcaire du Jurassique supérieur (Est du bassin de Paris). Compt. Rendus Geosci. 338, 931–941. https://doi.org/10.1016/j.crte.2006.06.005.

André, G., Hibsch, C., Fourcade, S., Cathelineau, M., Buschaert, S., 2010. Chronology of fracture sealing under a meteoric fluid environment: microtectonic and isotopic evidence of major Cainozoic events in the eastern Paris Basin (France). Tectonophysics 490, 214–228. https://doi.org/10.1016/j.tecto.2010.05.016.

Argus, D.F., Peltier, W.R., 2010. Constraining models of postglacial rebound using space geodesy: a detailed assessment of model ICE-5G (VM2) and its relatives. Geophys. J. Int. 181, 697–723. https://doi.org/10.1111/j.1365-246X.2010.04562.x.

Artemieva, I.M., 2019. Lithosphere structure in Europe from thermal isostasy. Earth Sci. Rev. 188, 454–468. https://doi.org/10.1016/j.earscirev.2018.11.004.

Artemieva, I., Thybo, H., Kaban, M., 2006. Deep Europe today: geophysical synthesis of the upper mantle structure and lithospheric processes over 3.5 Ga. Geol. Soc. Lond. Mem. 32, 11–41. https://doi.org/10.1144/GSL.MEM.2006.032.01.02.

Audet, P., 2014. Toward mapping the effective elastic thickness of planetary lithospheres from a spherical wavelet analysis of gravity and topography. Phys. Earth Planet. Inter. 226, 48–82. https://doi.org/10.1016/j.pepi.2013.09.011.

Bagge, M., Klemann, V., Steinberger, B., Latinović, M., Thomas, M., 2021. Glacial-isostatic adjustment models using geodynamically constrained 3D Earth structures. Geochem. Geophys. Geosyst. 22 https://doi.org/10.1029/2021GC009853 e2021GC009853.

Baykiev, E., Guerri, M., Fullea, J., 2018. Integrating gravity and surface elevation with magnetic data: mapping the Curie temperature beneath the British Isles and surrounding areas. Front. Earth Sci. 6.

BCSF RENASS, 2022. franceseisme.fr [WWW Document]. URL. https://renass.unistra.fr/fr/zones/ (accessed 7.7.22).

Beccaletto, L., Hanot, F., Serrano, O., Marc, S., 2011. Overview of the subsurface structural pattern of the Paris Basin (France): insights from the reprocessing and interpretation of regional seismic lines. In: Marine and Petroleum Geology, Thematic Set on the Implications of Basin Dynamics on Petroleum Systems, 28, pp. 861–879. https://doi.org/10.1016/j.marpetgeo.2010.11.006.

Blaise, T., Khoudja, S., Carpentier, C., Brigaud, B., Missenard, Y., Mangenot, X., Boulvais, P., Landrein, P., Cochard, J., 2022. Far-field brittle deformation record in the eastern Paris Basin (France). Geol. Mag. 1–15. https://doi.org/10.1017/S0016756822000772.

Brandes, C., Winsemann, J., Roskosch, J., Meinsen, J., Tanner, D.C., Frechen, M., Steffen, H., Wu, P., 2012. Activity along the Osning thrust in Central Europe during the Lateglacial: ice-sheet and lithosphere interactions. Quat. Sci. Rev. 38, 49–62. https://doi.org/10.1016/j.quascirev.2012.01.021.

Brandes, C., Steffen, H., Steffen, R., Wu, P., 2015. Intraplate seismicity in northern Central Europe is induced by the last glaciation. Geology 43. https://doi.org/10.1130/G36710.1.

Brudy, M., Zoback, M.D., Fuchs, K., Rummel, F., Baumgärtner, J., 1997. Estimation of the complete stress tensor to 8 km depth in the KTB scientific drill holes: implications for crustal strength. J. Geophys. Res. Solid Earth 102, 18453–18475. https://doi.org/10.1029/96JB02942.

Bureau des Recherches Géologiques et Minières (BRGM), 1996. Geological Map of France, Scale 1:1,000,000.

Burov, E.B., Diament, M., 1995. The effective elastic thickness (T e) of continental lithosphere: what does it really mean? J. Geophys. Res. Solid Earth 100, 3905–3927. https://doi.org/10.1029/94JB02770.

Byerlee, J., 1978. Friction of Rocks, 116, p. 12.

Calais, E., Freed, A., Arsdale, R., Stein, S., 2010. Triggering of new Madrid seismicity by late-pleistocene erosion. Nature 466, 608–611. https://doi.org/10.1038/nature09258.

Calais, E., Camelbeeck, T., Stein, S., Liu, M., Craig, T., 2016. A new paradigm for large earthquakes in stable continental plate interiors. Geophys. Res. Lett. 43 https://doi.org/10.1002/2016GL070815.

Cara, M., Cansi, Y., Schlupp, A., Arroucau, P., Béthoux, N., Beucler, E., Bruno, S., Calvet, M., Chevrot, S., Deboissy, A., Delouis, B., Denieul, M., Deschamps, A., Doubre, C., Fréchet, J., Godey, S., Golle, O., Grunberg, M., Guilbert, J., Woerd, K., 2015. SI-Hex: a new catalogue of instrumental seismicity for metropolitan France. Bull. Soc. Geol. Fr. 186, 3–19. https://doi.org/10.2113/gssgfbull.186.1.3.

Cazes, M., Mascle, A., Torreilles, X., Bois, C., Damotte, X., Matte, P., Raoult, X., Pham, V. N., Hirn, A., Galdeano, X., 1986. Large Variscan overthrusts beneath the Paris Basin. Nature 323, 144–147. https://doi.org/10.1038/323144a0.

Chamorro, C.R., García-Cuesta, J.L., Mondéjar, M.E., Pérez-Madrazo, A., 2014. Enhanced geothermal systems in Europe: an estimation and comparison of the technical and sustainable potentials. Energy 65, 250–263. https://doi.org/10.1016/j.energy.2013.11.078.

Clark, D., McPherson, A., Allen, T., 2014. Intraplate earthquakes in Australia. In: Intraplate Earthquakes, pp. 8–49. https://doi.org/10.1017/CBO9781139628921.003.

Cloetingh, S., Ziegler, P.A., Bogaard, P., Andriessen, P., Artemieva, I., Bada, G., Van Balen, R., Beekman, F., Ben-Avraham, Z., Brun, J.-P., Bunge, H., Burov, E., Carbonell, R., Facenna, C., Friedrich, A., Gallart, J., Green, A.G., Heidbach, O., Jones, A., Wolf, D., 2007. TOPO-EUROPE: the geoscience of coupled deep Earth-surface processes. Glob. Planet. Chang. 58, 1–118. https://doi.org/10.1016/j.gloplacha.2007.02.008.

Courboulex, F., Vallée, M., Causse, M., Chounet, A., 2016. Stress-drop variability of shallow earthquakes extracted from a global database of source time functions. Seismol. Res. Lett. 87, 912–918. https://doi.org/10.1785/0220150283.

Crone, A., De Martini, P.M., Machette, M., Okumura, K., Prescott, J., 2003. Paleoseismicity of two historically quiescent faults in Australia: implications for fault behavior in stable continental regions. Bull. Seismol. Soc. Am. 93, 1913–1934. https://doi.org/10.1785/0120000094.

Di Donato, G., Mitrovica, J.X., Sabadini, R., Vermeersen, L.L.A., 2000. The influence of a ductile crustal zone on glacial isostatic adjustment: geodetic observables along the U. S. East Coast. Geophys. Res. Lett. 27, 3017–3020. https://doi.org/10.1029/2000GL011390.

Dziewonski, A.M., Anderson, D.L., 1981. Preliminary reference Earth model. Phys. Earth Planet. Inter. 25, 297–356. https://doi.org/10.1016/0031-9201(81)90046-7.

EPOS, 2022. EPOS GNSS [WWW Document]. URL. https://gnss-epos.eu/ (accessed 1.31.22).
Etlicher, B., de Goër De Hervé, A., 1988. La déglaciation würmienne dans le Massif Central français, le point des travaux récents / The Würmian déglaciation in the French Massif-Central, review of recent works. Quaternaire 25, 103–110. https://doi.org/10.3406/quate.1988.1871.
Fenton, C.H., Adams, J., Halchuk, S., 2006. Seismic hazards assessment for radioactive waste disposal sites in regions of low seismic activity. Geotech. Geol. Eng. 24, 579–592. https://doi.org/10.1007/s10706-005-1148-4.
Forte, A.M., Mitrovica, J.X., Moucha, R., Simmons, N.A., Grand, S.P., 2007. Descent of the ancient Farallon slab drives localized mantle flow below the New Madrid seismic zone. Geophys. Res. Lett. 34 https://doi.org/10.1029/2006GL027895.
Grollimund, B., Zoback, M.D., 2001. Did deglaciation trigger intraplate seismicity in the New Madrid seismic zone? Geology 29, 175–178. https://doi.org/10.1130/0091-7613(2001)029<0175:DDTISI>2.0.CO;2.
Guillocheau, F., Robin, C., Allemand, P., Bourquin, S., Brault, N., Dromart, G., Friedenberg, R., Garcia, J., Gaulier, J.-M., Gaumet, F., Grosdoy, B., Hanot, F., 2000. Meso-Cenozoic geodynamic evolution of the Paris Basin: 3D stratigraphic constraints. Geodin. Acta 13, 189–245. https://doi.org/10.1080/09853111.2000.11105372.
Hampel, A., Hetzel, R., Maniatis, G., Karow, T., 2009. Three-dimensional numerical modeling of slip rate variations on normal and thrust fault arrays during ice cap growth and melting. J. Geophys. Res. Solid Earth 114. https://doi.org/10.1029/2008JB006113.
Hampel, A., Karow, T., Maniatis, G., Hetzel, R., 2010. Slip rate variation on faults during glacial loading and post-glacial unloading: implications for the viscosity structure of the lithosphere. J. Geol. Soc. Lond. 167, 385–399. https://doi.org/10.1144/0016-76492008-137.
Haskell, N.A., 1937. The viscosity of the asthenosphere. Am. J. Sci. s5-33, 22–28. https://doi.org/10.2475/ajs.s5-33.193.22.
Heidbach, O., Rajabi, M., Reiter, K., Ziegler, M., WSM Team, 2016. World Stress Map Database Release 2016. https://doi.org/10.5880/WSM.2016.001.
Hough, S., Page, M., 2011. Toward a consistent model for strain accrual and release for the New Madrid Seismic Zone, Central United States. J. Geophys. Res. 116 https://doi.org/10.1029/2010JB007783.
Hough, S.E., Seeber, L., Armbruster, J.G., 2003. Intraplate triggered earthquakes: observations and interpretation. Bull. Seismol. Soc. Am. 93, 2212–2221. https://doi.org/10.1785/0120020055.
Houtgast, R.F., Van Balen, R.T., Kasse, C., 2005. Late Quaternary evolution of the Feldbiss Fault (Roer Valley Rift System, the Netherlands) based on trenching, and its potential relation to glacial unloading. In: Quaternary Science Reviews, Neotectonics and Quaternary Fault-Reactivation in Europe's Intrap Late Lithosphere, 24, pp. 489–508. https://doi.org/10.1016/j.quascirev.2004.01.012.
ICONS, 2022. ICONS Basin Atlas: European Region [WWW Document]. URL. https://www.earthbyte.org/Resources/ICONS/EUR/EUR.2m.html (accessed 2.2.22).
IRSN, 2022. BDFA [WWW Document]. URL. https://bdfa.irsn.fr/ (accessed 10.26.22).
Ivy-Ochs, S., Kerschner, H., Reuther, A., Preusser, F., Heine, K., Maisch, M., Kubik, P.W., Schlüchter, C., 2008. Chronology of the last glacial cycle in the European Alps. J. Quat. Sci. 23, 559–573. https://doi.org/10.1002/jqs.1202.
Jackson, J., McKenzie, D., 2022. The exfoliation of cratonic Australia in earthquakes. Earth Planet. Sci. Lett. 578, 117305 https://doi.org/10.1016/j.epsl.2021.117305.
Johnston, A.C., 1989. The seismicity of 'stable continental interiors'. In: Earthquakes at North-Atlantic Passive Margins: Neotectonics and Postglacial Rebound. Springer Netherlands, Dordrecht, pp. 299–327. https://doi.org/10.1007/978-94-009-2311-9_18.
Johnston, A.C., Kanter, L.R., Coppersmith, K.J., Cornell, C.A., 1994. The earthquakes of stable continental regions. Volume 1, assessment of large earthquake potential. In: Final Report (No. EPRI-TR-102261-V1). Electric Power Research Inst. (EPRI), Palo Alto, CA (United States); Memphis State Univ., TN (United States). Center for Earthquake Research and Information; Geomatrix Consultants, Inc., San Francisco, CA (United States); Cornell (C.A.), Portola Valley, CA (United States).
Kaban, M.K., Chen, B., Tesauro, M., Petrunin, A.G., Khrepy, S.E., Al-Arifi, N., 2018. Reconsidering effective elastic thickness estimates by incorporating the effect of sediments: a case study for Europe. Geophys. Res. Lett. 45, 9523–9532. https://doi.org/10.1029/2018GL079732.
Kaufmann, G., Amelung, F., 2000. Reservoir-induced deformation and continental rheology in vicinity of Lake Mead, Nevada. J. Geophys. Res. 105, 16341–16358. https://doi.org/10.1029/2000JB900079.
Klemann, V., Wu, P., Wolf, D., 2003. Compressible viscoelasticity: stability of solutions for homogeneous plane-Earth models. Geophys. J. Int. 153, 569–585. https://doi.org/10.1046/j.1365-246X.2003.01920.x.
Klose, C., Seeber, L., 2007. Shallow seismicity in stable continental regions. Seismol. Res. Lett. 78, 554–562. https://doi.org/10.1785/gssrl.78.5.554.
Lahtinen, R., Korja, A., Nironen, M., 2005. Palaeoproterozoic tectonic evolution of the Fennoscandian Shield. Precambrian geology of Finland -key to the evolution of the Fennoscandian Shield. Dev. Precambrian Geol. 14, 418–532.
Lambeck, K., Purcell, A., Zhao, S., 2017. The North American late Wisconsin ice sheet and mantle viscosity from glacial rebound analyses. Quat. Sci. Rev. 158, 172–210. https://doi.org/10.1016/j.quascirev.2016.11.033.
Lambert, A., Courtier, N., Sasagawa, G., Klopping, F., Winester, D., James, T., Liard, J., 2001. New constraints on Laurentide postglacial rebound from absolute gravity measurements. Geophys. Res. Lett. 28, 2109–2112. https://doi.org/10.1029/2000GL012611.
Lucazeau, F., Vasseur, G., 1989. Heat flow density data from France and surrounding margins. Tectonophysics 164, 251–258. https://doi.org/10.1016/0040-1951(89)90018-8.
Lund, B., 2005. Effects of Deglaciation on the Crustal Stress Field and Implications for Endglacial Faulting: A Parametric Study of Simple Earth and Ice Models (No. 1404–0344). Sweden.
Majorowicz, J., Wybraniec, S., 2011. New terrestrial heat flow map of Europe after regional paleoclimatic correction application. Int. J. Earth Sci. 100, 881–887. https://doi.org/10.1007/s00531-010-0526-1.
Majorowicz, J., Polkowski, M., Grad, M., 2019. Thermal properties of the crust and the lithosphere–asthenosphere boundary in the area of Poland from the heat flow variability and seismic data. Int. J. Earth Sci. (Geol. Rundsch.) 108, 649–672. https://doi.org/10.1007/s00531-018-01673-8.
Masson, C., 2019. Perfectionnement des méthodes d'analyse GPS pour l'étude de la déformation intraplaque: cas de la France (These de doctorat). Montpellier.
Masson, C., Mazzotti, S., Vernant, P., Doerflinger, E., 2019. Extracting small deformation beyond individual station precision from dense global navigation satellite system (GNSS) networks in France and western Europe. Solid Earth 10, 1905–1920. https://doi.org/10.5194/se-10-1905-2019.
Matte, P., Hirn, A., 1988. Seismic signature and tectonic cross section of the Variscan crust in western France. Tectonics 7, 141–155. https://doi.org/10.1029/TC007i002p00141.
Mazzotti, S., 2007. Geodynamic models for earthquake studies in intraplate North America. In: Special Paper of the Geological Society of America, pp. 17–33. https://doi.org/10.1130/2007.2425(02).
Mazzotti, S., Gueydan, F., 2018. Control of tectonic inheritance on continental intraplate strain rate and seismicity. In: Tectonophysics, Understanding Geological Processes Through Modelling - A Memorial Volume Honouring Evgenii Burov, 746, pp. 602–610. https://doi.org/10.1016/j.tecto.2017.12.014.
Mazzotti, S., Jomard, H., Masson, F., 2020. Processes and deformation rates generating seismicity in metropolitan France and conterminous Western Europe. BSGF - Earth Sci. Bull. 191, 19. https://doi.org/10.1051/bsgf/2020019.
Mazzotti, S., Aubagnac, C., Bollinger, L., Coca Oscanoa, K., Delouis, B., Do Paco, D., Doubre, C., Godano, M., Jomard, H., Larroque, C., Laurendeau, A., Masson, F., Sylvander, M., Trilla, A., 2021. FMHex20: an earthquake focal mechanism database for seismotectonic analyses in metropolitan France and bordering regions. Bulletin de la Société Géologique de France 192, 10. https://doi.org/10.1051/bsgf/2020049.
Mégnien, C., 1980. Synthèse géologique du Bassin de Paris. Mém. BRGM, p. 101.
Mey, J., Scherler, D., Wickert, A.D., Egholm, D.L., Tesauro, M., Schildgen, T.F., Strecker, M.R., 2016. Glacial isostatic uplift of the European Alps. Nat. Commun. 7 https://doi.org/10.1038/ncomms13382.
Mörner, N.-A., 1978. Faulting, fracturing, and seismicity as functions of glacio-isostasy in Fennoscandia. Geology 6, 41. https://doi.org/10.1130/0091-7613(1978)6<41:FFASAF>2.0.CO;2.
Muir-Wood, R., 2000. Deglaciation seismotectonics: a principal influence on intraplate seismogenesis at high latitudes. Quat. Sci. Rev. 19, 1399–1411. https://doi.org/10.1016/S0277-3791(00)00069-X.
Nurmi, P., Oy, 2021. Preliminary Evaluation of the Estonian Geoenergy Potential and Overview of Available Technologies, Expert Opinion for using those Technologies in the Estonian Geological Conditions, Suggestions for Possible Further Actions and Examples of Case Studies.
Patton, H., Hubbard, A., Andreassen, K., Auriac, A., Whitehouse, P.L., Stroeven, A.P., Shackleton, C., Winsborrow, M., Heyman, J., Hall, A.M., 2017. Deglaciation of the Eurasian ice sheet complex. Quat. Sci. Rev. 169, 148–172. https://doi.org/10.1016/j.quascirev.2017.05.019.
Peltier, W.R., 1974. The impulse response of a Maxwell Earth. Rev. Geophys. 12, 649–669. https://doi.org/10.1029/RG012i004p00649.
Ranalli, G., 1994. Nonlinear flexure and equivalent mechanical thickness of the lithosphere. Tectonophysics 240, 107–114. https://doi.org/10.1016/0040-1951(94)90266-6.
Rossi, F., Baudouy, L., 2015. Modèle structural régional et local révisé (No. F. RP.0GTR.14.0004). ANDRA.
Schmidt, P., Lund, B., Hieronymus, C., 2012. Implementation of the glacial rebound prestress advection correction in general-purpose finite element analysis software: springs versus foundations. Comput. Geosci. 40 https://doi.org/10.1016/j.cageo.2011.07.017.
Schotman, H.H.A., Wu, P., Vermeersen, L.L.A., 2008. Regional perturbations in a global background model of glacial isostasy. In: Physics of the Earth and Planetary Interiors, Recent Advances in Computational Geodynamics: Theory, Numerics and Applications, 171, pp. 323–335. https://doi.org/10.1016/j.pepi.2008.02.010.
Schulte, S.M., Mooney, W.D., 2005. An updated global earthquake catalogue for stable continental regions: reassessing the correlation with ancient rifts. Geophys. J. Int. 161, 707.
Seguinot, J., Ivy-Ochs, S., Jouvet, G., Huss, M., Funk, M., Preusser, F., 2018. Modelling last glacial cycle ice dynamics in the Alps. Cryosphere 12, 3265–3285. https://doi.org/10.5194/tc-12-3265-2018.
Singh, S.K., Pacheco, J., Bansal, B.K., Pérez-Campos, X., Dattatrayam, R., Suresh, C., 2004. A source study of the Bhuj, India, earthquake of 26 January 2001 (M_w 7.6). Bull. Seismol. Soc. Am. 94.
Spada, G., Barletta, V.R., Klemann, V., Riva, R.E.M., Martinec, Z., Gasperini, P., Lund, B., Wolf, D., Vermeersen, L.L.A., King, M.A., 2011. A benchmark study for glacial isostatic adjustment codes. Geophys. J. Int. 185, 106–132. https://doi.org/10.1111/j.1365-246X.2011.04952.x.
Steffen, H., Kaufmann, G., 2005. Glacial isostatic adjustment of Scandinavia and northwestern Europe and the radial viscosity structure of the Earth's mantle. Geophys. J. Int. 163, 801–812. https://doi.org/10.1111/j.1365-246X.2005.02740.x.
Steffen, H., Kaufmann, G., Wu, P., 2006. Three-dimensional finite-element modeling of the glacial isostatic adjustment in Fennoscandia. Earth and Planet. Sci. Lett. 250 (1–2), 358–375. https://doi.org/10.1016/j.epsl.2006.08.003. ISSN 0012-821X.

Steffen, R., Steffen, H., 2021. Reactivation of non-optimally orientated faults due to glacially induced stresses. Tectonics 40. https://doi.org/10.1029/2021TC006853 e2021TC006853.
Steffen, R., Steffen, H., Wu, P., Eaton, D.W., 2014. Stress and fault parameters affecting fault slip magnitude and activation time during a glacial cycle. Tectonics 33, 1461–1476. https://doi.org/10.1002/2013TC003450.
Steffen, R., Steffen, H., Wu, P., Eaton, D.W., 2015. Reply to comment by Hampel et al. on "Stress and fault parameters affecting fault slip magnitude and activation time during a glacial cycle". Tectonics 34, 2359–2366. https://doi.org/10.1002/2015TC003992.
Stein, S., Mazzotti, S., 2007. Continental Intraplate Earthquakes: Science, Hazard, and Policy Issues. Geological Society of America.
Stein, R.S., King, G.C.P., Lin, J., 1992. Change in failure stress on the Southern San Andreas fault system caused by the 1992 magnitude = 7.4 landers earthquake. Science 258, 1328–1332. https://doi.org/10.1126/science.258.5086.1328.
Štěpančíková, P., Rockwell, T.K., Stemberk, J., Rhodes, E.J., Hartvich, F., Luttrell, K., Myers, M., Táborík, P., Rood, D.H., Wechsler, N., Nývlt, D., Ortuño, M., Hók, J., 2022. Acceleration of late Pleistocene activity of a central European fault driven by ice loading. Earth Planet. Sci. Lett. 591, 117596 https://doi.org/10.1016/j.epsl.2022.117596.
Stewart, I., Sauber, J., Rose, J., 2000. Glacio-seismotectonics: ice sheets, crustal deformation and seismicity. Quat. Sci. Rev. 19, 1367–1389. https://doi.org/10.1016/S0277-3791(00)00094-9.
Talwani, P., 2017. On the nature of intraplate earthquakes. J. Seismol. 21 https://doi.org/10.1007/s10950-016-9582-8.
Tarayoun, A., Mazzotti, S., Craymer, M., Henton, J., 2018. Structural inheritance control on intraplate present-day deformation: GPS strain rate variations in the Saint Lawrence Valley, Eastern Canada. J. Geophys. Res. Solid Earth. https://doi.org/10.1029/2017JB015417.
Tarayoun, A., Mazzotti, S., Gueydan, F., 2019. Quantitative impact of structural inheritance on present-day deformation and seismicity concentration in intraplate deformation zones. Earth Planet. Sci. Lett. 518, 160–171. https://doi.org/10.1016/j.epsl.2019.04.043.
Tesauro, M., Kaban, M.K., Cloetingh, S.A.P.L., 2008. EuCRUST-07: a new reference model for the European crust. Geophys. Res. Lett. 35 https://doi.org/10.1029/2007GL032244.
Tesauro, M., Kaban, M.K., Cloetingh, S.A.P.L., 2009a. How rigid is Europe's lithosphere? Geophys. Res. Lett. 36 https://doi.org/10.1029/2009GL039229.
Tesauro, M., Kaban, M.K., Cloetingh, S.A.P.L., 2009b. A new thermal and rheological model of the European lithosphere. Tectonophysics 476, 478–495. https://doi.org/10.1016/j.tecto.2009.07.022.
Tesauro, M., Audet, P., Kaban, M.K., Cloetingh, S., 2012a. The effective elastic thickness of the continental lithosphere: comparison between rheological and inverse approaches. Geochem. Geophys. Geosyst. 13 https://doi.org/10.1029/2012GC004162.
Tesauro, M., Kaban, M.K., Cloetingh, S.A.P.L., 2012b. Global strength and elastic thickness of the lithosphere. In: Global and Planetary Change, Coupled Deep Earth and Surface Processes in System Earth: Monitoring, Reconstruction and Process Modeling, 90–91, pp. 51–57. https://doi.org/10.1016/j.gloplacha.2011.12.003.
Tesauro, M., Kaban, M.K., Cloetingh, S.A.P.L., 2013. Global model for the lithospheric strength and effective elastic thickness. Tectonophysics 602, 78–86. https://doi.org/10.1016/j.tecto.2013.01.006. Topo-Europe III.
Townend, J., Zoback, M.D., 2000. How faulting keeps the crust strong. Geology 28, 399–402. https://doi.org/10.1130/0091-7613(2000)28<399:HFKTCS>2.0.CO;2.
Turcotte, D.L., Schubert, G., 2002. Geodynamics, 2nd ed. Cambridge University Press, Cambridge. https://doi.org/10.1017/CBO9780511807442.
Turpeinen, H., Hampel, A., Karow, T., Maniatis, G., 2008. Effect of ice growth and melting on the slip evolution of thrust faults. Earth Planet. Sci. Lett. 269, 230–241. https://doi.org/10.1016/j.epsl.2008.02.017.
Tushingham, A., Peltier, W., 1992. Validation of the ICE-3G model of Würm-Wisconsin deglaciation using a global data base of relative sea level histories. J. Geophys. Res. 97, 3285–3304. https://doi.org/10.1029/91JB02176.
Vachon, R., Schmidt, P., Lund, B., Plaza, A., Patton, H., Hubbard, A., 2022. Glacially induced stress across the Arctic from the Eemian interglacial to the present - implications for faulting and methane seepage. J. Geophys. Res. Solid Earth 127. https://doi.org/10.1029/2022JB024272.
Van der Wal, W., Barnhoorn, A., Stocchi, P., Gradmann, S., Wu, P., Drury, M., Vermeersen, B., 2013. Glacial isostatic adjustment model with composite 3-D Earth rheology for Fennoscandia. Geophys. J. Int. 194 (1), 61–77. https://doi.org/10.1093/gji/ggt099.
Veikkolainen, T., Kukkonen, I., Tiira, T., 2017. Heat flow, seismic cutoff depth and thermal modeling of the Fennoscandian Shield. Geophys. J. Int. 211, 1414–1427. https://doi.org/10.1093/gji/ggx373.
Watts, A., Zhong, S., 2002. Observations of flexure and the rheology of oceanic lithosphere. Geophys. J. Int. 142, 855–875. https://doi.org/10.1046/j.1365-246x.2000.00189.x.
Wickert, A., 2015. Open-source modular solutions for flexural isostasy: gFlex v1.0. Geosci. Model Dev. Discuss. 8, 4245–4292. https://doi.org/10.5194/gmdd-8-4245-2015.
Wileveau, Y., Cornet, F.H., Desroches, J., Blumling, P., 2007. Complete in situ stress determination in an argillite sedimentary formation. Phys. Chem. Earth 32, 866–878. https://doi.org/10.1016/j.pce.2006.03.018.
Wu, P., 2004. Using commercial finite element packages for the study of earth deformations, sea levels and the state of stress. Geophys. J. Int. 158, 401–408. https://doi.org/10.1111/j.1365-246X.2004.02338.x.
Wu, P., Johnston, P., 1998. Validity of using Flat-Earth Finite Element Models in the study of Postglacial Rebound, pp. 191–202.
Wu, P., Johnston, P., 2000. Can deglaciation trigger earthquakes in N. America? Geophys. Res. Lett. 27, 1323–1326. https://doi.org/10.1029/1999GL011070.
Wu, P., Mazzotti, S., 2007. Effects of a lithospheric weak zone on postglacial seismotectonics in Eastern Canada and Northeastern USA. In: Special Paper of the Geological Society of America, pp. 113–128. https://doi.org/10.1130/2007.2425(09).
Zhang, Z., Chen, J., Lin, J., 2008. Stress interactions between normal faults and adjacent strike-slip faults of 1997 Jiashi earthquake swarm. Sci. China Ser. D Earth Sci. 51, 431–440. https://doi.org/10.1007/s11430-008-0023-6.
Zoback, M.D., Healy, J.H., 1992. In situ stress measurements to 3.5 km depth in the Cajon Pass scientific research borehole: implications for the mechanics of crustal faulting. J. Geophys. Res. 97, 5039.